Imaging with Mass Spectrometry

M. L. Pacholski and N. Winograd*

Department of Chemistry, Penn State University, 184 Materials Research Institute Building, University Park, Pennsylvania 16802

Received February 16, 1999 (Revised Manuscript Received May 18, 1999)

Contents

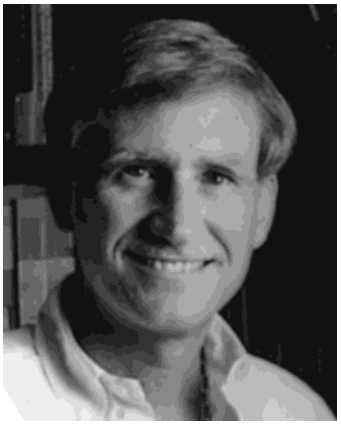

Nicholas Winograd was born on December 27, 1945, in New London, CT. In 1967 he received his B.S. in Chemistry from Rensselaer Polytechnic Institute in Troy, NY. At Case Western Reserve University in Cleveland, OH, he received his Ph.D. in 1970 under the direction of Prof. Theodore Kuwana. He joined the Chemistry Faculty at Purdue University in 1970 as an Assistant Professor and was promoted to Associate Professor in 1975. In 1979 he moved to Penn State University, accepting a position as Professor of Chemistry, and was named Evan Pugh Professor 1985. As mass spectrometry has become an important tool for the study of biomolecules, Winograd has become fascinated with the use of focused ion beams for molecule-specific imaging experiments, especially using biomaterials.

Michaeleen L. Pacholski was born in Buffalo, NY, on March 5, 1973. She received her B.S. in Chemistry from the State University of New York at Buffalo in 1994. She recently completed her Ph.D. degree under the direction of Nicholas Winograd at Penn State University. Her thesis work focused on chemical imaging of biological and model biological systems using time-of-flight secondary ion mass spectrometry. She is now employed in the Surface Science Division of Rohm and Haas in Spring House, PA.

I. Introduction

Imaging mass spectrometry (MS) has created new fundamental research opportunities in many fields because of its unique ability to acquire molecule- and element-specific pictures on a submicron spatial regime. Moreover, since recent advances in mass spectrometry allow analysis of polymers, metals, oxides, thermally labile biomolecules, and other solid state materials, numerous applications have emerged in such diverse fields as biotechnology, microelectronics, materials science, geochemistry, and surface analysis. Indeed, the push to fabricate nanometer scale devices and to miniaturize many aspects of scientific research has mandated the need for tech-

10.1021/cr980137w CCC: $35.00
Published on Web 09/15/1999

niques which provide chemically selective information on a small scale. These needs have also driven the MS community to improve the sensitivity and the ultimate spatial resolution of imaging techniques.

Mass spectrometry is not normally thought to provide spatially resolved information. The first to conceive of such an idea were Castaing and Slodzian, more than 35 years ago.[1] They created ions by bombarding solids with energetic particles of several dozen kiloelectronvolts of kinetic energy. Masses of the ejected species were directly measured utilizing a magnetic analyzer. These species are termed secondary ions and their mass analysis forms the basis for secondary ion mass spectrometry (SIMS). Castaing and Slodzian reasoned that it should be possible to build an ion−optical collection system, analogous to a lens used in a light microscope, to preserve the spatial relationship of the desorbed ions from sample to detector.

Largely due to the commercialization of this instrumentation, the ion microscope quickly became a widely used tool in many fields. Early studies utilized the element-specific characteristics provided by the mass analyzer to characterize the distribution of metals in alloys.[1] Other efforts used the ion microscope in biology to try to map the spatial distribution of characteristic ions in root cap tissue samples.[2] In catalysis, elemental distributions of metals in fluid cracking catalysts were assayed.[3]

The ion microscope concept is complementary with a more direct approach of imaging by rastering a focused ion beam across the target.[4] This strategy places fewer restrictions on the nature of mass analyzers and has become popular recently primarily due to the development of the liquid metal ion gun (LMIG). The beam eminating from this ion source can be focused onto the target with a diameter of less than 20 nm, providing very high lateral resolution of element-specific images.[5] In addition, the idea of imaging molecular species desorbed from a surface by a focused ion beam has come into play. This notion was made possible by the early discovery that molecular ions, as well as elemental ions, are seen in the mass spectra if the primary ion dose is kept below certain limits.[6] To analyze a much larger mass range, time-of-flight mass analyzers were implemented.[7] They increased the detection efficiency by several orders of magnitude over the traditional analyzers.

A modern experimental configuration, termed imaging time-of-flight secondary ion mass spectrometry (imaging TOF-SIMS), exhibits remarkable characteristics. Using a 25 keV Ga^+ ion LMIG, for example, these instruments produce spatially resolved images of molecular species with molecular weights up to several thousand daltons and with a spatial resolution less than 100 nm.[8] As we shall see, the numbers suggest that the mass spectra are being acquired from just a few thousand molecules.

As applications of molecular imaging experiments continue to expand, new variants of the experimental protocol are promising further breakthroughs. For example, it is possible to improve the yield of molecular ions using cluster ion beam sources rather than atomic ion sources.[9,10] A group of projectile atoms can more efficiently desorb labile molecules with less fragmentation than a single atomic ion. Another development referred to as secondary neutral MS (SNMS) involves the use of electron beams[11] or laser beams[12] to ionize neutral molecules desorbed from the surface by the primary ion beam. Since this scheme separates ionization from desorption, it has also been termed postionization. Preliminary laser ionization studies have been shown to increase measured ion signals by 10−100-fold.[13] Finally, a few investigators are examining the use of focused laser beam probes to desorb large biomolecules, albeit with lower spatial resolution.[14] These experiments take advantage of remarkable advances in matrix-assisted laser desorption ionization (MALDI) mass spectrometry which allow detection of proteins and nucleotides of several hundred thousand daltons.

Many reviews have been written concerning mass spectrometry and imaging. Two good general books about SIMS have been written by Benninghoven[15] and Vickerman.[16] In addition, there are reviews concerning SIMS,[17−22] imaging SIMS,[23−27] biological SIMS,[28−31] postionization,[22,24,32−34] and SIMS of polymers.[35] A comparison of various microanalysis techniques with SIMS is also available.[36] In this review we discuss a number of the critical and experimental issues associated with imaging mass spectrometry. Of special interest will be the possibilities for molecule-specific imaging and the inherent limitations associated with this strategy. In addition, we review a number of the recent applications of imaging MS, with an emphasis on illustrating the broad range of materials that are amenable to study.

II. Experimental Considerations and Instrumentation

Mass spectral imaging is almost exclusively performed using ion beam induced desorption. In this mode, an incident ion beam consisting of O_2^+, Cs^+, or Ga^+ is focused to a probe size of a few nanometers to a few hundred nanometers.[37] The masses of the desorbed ions are then measured with a magnetic sector, quadrupole, or time-of-flight mass analyzer. An image is collected by sequentially scanning the probe within the image area and collecting a mass spectrum at each pixel. The magnitude of the incident ion dose establishes whether a dynamic or static SIMS experiment is being performed. Both strategies have been implemented in the ion microscope mode as well.

For dynamic SIMS, the number of incident ions exceeds the number of surface atoms on the sample, which results in erosion due to sputtering and chemical damage to the surface. By acquiring images as a function of time, however, elemental information may be obtained as a function of depth into the sample. With a typical beam current of 10^{-9} A incident on a 1 μm^2 area (10^{-1} A/cm^2), for example, 6 $\times$ 10^9 primary ions strike 10^7 substrate atoms each second. Assuming that about 10 surface atoms desorb for each incident ion, the erosion rate is several microns per minute. Depending upon the fraction of desorbed species that are ionized, and their surface

concentration, it is possible to acquire several thousand ions per pixel.

In contrast, static SIMS measurements, as first promoted by Benninghoven in 1973, are performed such that the number of incident ions is about an order of magnitude less than the number of surface atoms.[6] For the example discussed above, the same 10^{-9} A beam would exceed the static limit after only 10^{-3} s. In the static regime, on the other hand, both elemental and molecular species are desorbed from the surface. Chemical damage created by the incident ion beam probe is not typically observed since each incident ion has a high probability of striking an unperturbed part of the target. Because of the required low dose, images are usually acquired with only a few counts/pixel.

In summary, dynamic measurements primarily yield elemental information, three-dimensional or depth profiling capabilities, and relatively high count rates. For static measurements, it is possible to acquire molecular information about the imaged area, although count rates are quite low and the information content is restricted to only the surface layers.

A. Primary Ion Sources

The Ga^+ liquid metal ion gun (LMIG) currently provides the smallest probe size with the highest current density of any ion gun. This source was first coupled to MS experiments in the early 1980s[38] and optimized by the Levi-Setti group shortly thereafter by coupling an LMIG to a quadrupole mass analyzer.[39] Today, probe sizes of less than 10 nm with current densities of 1−10 A/cm^2 are routinely available.[40]

The LMIG normally consists of a field emitter tip coated with Ga. A high electric field extracts Ga^+ ions from the tip, and the ions are focused onto the sample via ion optics. To achieve the smallest probe sizes, the Ga^+ ion kinetic energy must be in the range of 20−60 keV. The operation of these sources is not unlike the field emission electron probe used in high-resolution scanning electron microprobes.

Several issues need to be considered when performing static or dynamic SIMS experiments. The first issue involves the damage that a single ion impact causes to the surface. It is known that a single incident projectile sets in motion a large number of atoms near the sample surface, a phenomenon described as the collision cascade.[41,42] Eventually some atoms in the cascade acquire momentum components which point away from the surface, leading to desorption, ionization, and ultimately detection. STM measurements on a Si{111} surface bombarded by a single 3 keV Ar^+ ion, for example, indicate that the damage area is on the order of ∼25 nm^2.[43−45]

These interactions have been modeled using molecular dynamics computer simulations. The calculations provide an atomic-level view of the motion that leads to desorption. A typical calculation for 25 keV Ar^+ ion bombardment of a metal single crystal is shown in Figure 1.[24] The results suggest that the desorption event is finished in ∼200 fs, most of the particles desorb from the top layer, and the disruption area extends about 5 nm from the impact point. Therefore, probe sizes smaller than about 20 nm will not provide better lateral resolution when performing MS imaging.

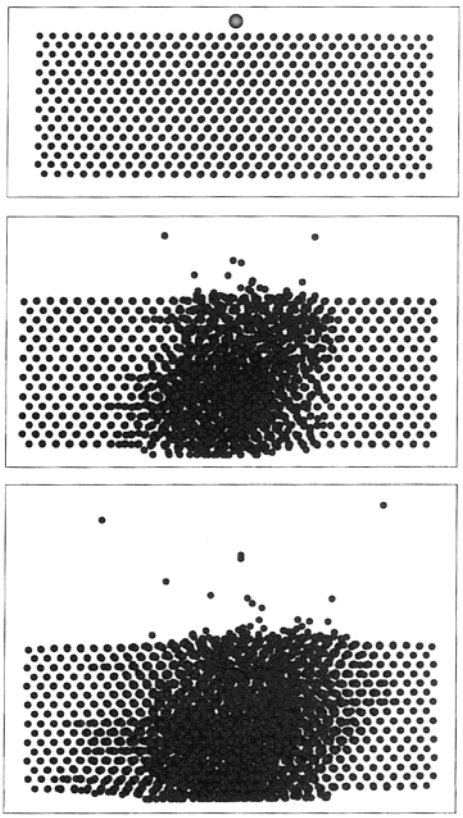

Figure 1. Time snapshots at 0 fs (top), 100 fs (middle), and 200 fs (bottom) from a molecular dynamics simulation for 25 keV Ar^+ ion bombardment of Rh metal. The view is from the side of a 60 Å microcrystallite containing 16 layers of ∼500 atoms per layer.[24]

Table 1. Useful Yields of Species M in a Steel Matrix under O_2^+, Ga^+, and Cs^+ Bombardment[37]

M	O_2^+ M^+	Ga^+ M^+	Cs^+ MCs^+
Si	2.0×10^{-3}	5.9×10^{-6}	1.6×10^{-5}
Cr	3.4×10^{-2}	2.5×10^{-4}	1.6×10^{-4}
Mn	2.3×10^{-2}	4.1×10^{-4}	4.2×10^{-4}
Fe	3.2×10^{-3}	4.7×10^{-4}	1.6×10^{-4}
Ni	7.9×10^{-4}	3.9×10^{-5}	3.3×10^{-5}
Cu	5.9×10^{-4}	1.8×10^{-5}	2.8×10^{-5}
Mo	7.7×10^{-3}	1.3×10^{-4}	8.4×10^{-5}

Another issue relates to the effectiveness of Ga^+ ions in desorbing ionized elemental or molecular species. Normally, for dynamic SIMS studies, bombardment is most effective with O_2^+ ions, to enhance positive ion formation, or Cs^+ ions, to enhance negative ion formation. A few examples are shown in Table 1.[37] The chemically reactive nature of these primary ions creates either electropositive or electronegative surface species which retain their charge during desorption.[46,47] Unfortunately, Ga^+ ions do not have this effect on ion yields and in fact produce comparably poor results, as shown in Table 1. Oxygen flooding during Ga^+ ion bombardment can increase ion yields, but for high-resolution imaging, the erosion rate of the sample is high and reacted O_2 is immediately sputtered from the surface, so the pres-

sure of O_2 cannot be increased enough to be helpful. Hence, Ga^+ ion beams are best utilized with materials which have inherently high ion yields.

For static SIMS imaging experiments, reactive ion beams are not appropriate since reactive gases are likely to change the molecular nature of the surface. Furthermore, reactive ion bombardment is not effective due to the low primary ion dose. As it turns out, Ga^+ ions are not particularly efficient projectiles for inducing molecular ion desorption, relative to other ions of heavier mass.[48] The high kinetic energies required for small spot sizes are not optimum, since many of the incident particles penetrate deeply into the target, causing no desorption at all. The Ga^+ ion gun, however, provides the best possible lateral resolution and brightness, making it the ion source of choice for high spatial resolution imaging MS experiments.

There are occasions where it is desirable to trade some of the spatial resolution associated with the Ga^+ LMIG by using other ion sources that produce high yields of molecular species. One such approach involves substitution of In for Ga as a source material. The difference in atomic mass of these two substances (115 amu vs 69 amu) is enough to enhance the molecular ion yield by a factor of 4−5 for many samples.[48] Difficulties include obtaining sub-100 nm probe sizes due to chromatic abberations during field emission of In^+ ions, oxidation of the emitter tip, and finding a source of isotopically pure In, which is needed for TOF applications. Another strategy is to utilize Au as a primary ion source. Gold cluster ions such as Au_2^+ and Au_3^+ can enhance the yield by more than 10-fold over Ga^+,[10] but as yet, Au sources with lifetimes greater than a few dozen hours have not been developed. Ion sources are a fruitful area for research since major improvements to the Ga^+ ion source would greatly expand possible applications of imaging MS experiments.

Other types of ion sources are available for dynamic SIMS imaging experiments. The most commonly used is the Cs^+ ion source. Ions are produced by surface ionization from a macroscopic Cs substrate, extracted through apertures and electronically focused onto the target. Although this source can produce high-quality beams with a diameter of 40 μm, it is not possible to achieve sub-100 nm spot sizes unless the current is reduced to an impractically low level.[37] Focused beams of rare gas ions (Ar^+ and Xe^+) or O_2^+ ions may be produced from duoplasmatron sources with similar characteristics as those reported for Cs^+.[49]

In summary, the Ga^+ LMIG provides the best possible lateral resolution of any known ion source, but does not yield the most molecular information about a surface. LMIGs which employ other elements such as In or Au, surface ionization Cs^+ ion sources, and duoplasmatron sources all provide improved mass spectra but considerably degrade image quality. It is interesting to note that recent studies have shown that unfocused cluster ion beam sources consisting of exotic materials such as C_{60}^+,[50] SF_5^+,[51] and Au_3^+ [10] ions produce even higher yields of molecular species. Molecular ion yields can be improved by more than an order of magnitude without increasing the damage cross section from such sources. It will be a future challenge to incorporate these cluster ions into devices that produce bright, tightly focused beams.

B. Mass Analyzers

There are three types of mass analyzers currently in use and commercially available for imaging MS experiments. These include the quadrupole mass analyzer (QMA), the double focusing magnetic sector, and the TOF analyzer. The latter device may be configured in a number of different geometries. There are many excellent reviews which describe the detailed characteristics and operation of each of these systems and we will not attempt to duplicate those efforts.[15,16,21,52] Rather, it is our purpose to emphasize the general characteristics of each of these devices, especially for imaging experiments, and to examine tradeoffs when choosing one type over the other.

The original static SIMS experiments reported in the 1970s were based upon QMAs because of their high transmission, compatibility with ultrahigh vacuum, and relative insensitivity to the kinetic energy of secondary ions. Moreover, the lens designs provided a large field of view of the analyzer, a critical factor since sample consumption was a major concern. Dynamic SIMS experiments, primarily from the Levi-Setti group, also incorporated the QMA with the Ga^+ ion LMIG for similar reasons.[53] During the 1980s, however, the emphasis shifted to the study of larger molecules by static SIMS and the limited mass range of the QMA proved too restrictive.

During this same period of time Chait and Standing noted that it was possible to achieve significant improvement in both mass resolution and transmission efficiency using the TOF approach.[7] In this configuration, the primary ions are directed toward the sample as a very short pulse. Desorbed molecular ions, of mass m, are accelerated to a specific energy and allowed to drift through a fixed distance x. Since the kinetic energy is defined as

$$E = {}^1/_2 mv^2 = {}^1/_2 mx^2/t^2 \qquad (1)$$

the arrival time t of the ion reveals its mass. The major advantage of the TOF analyzer is that it sequentially detects all ions with differing flight times and mass, rather than only one mass at a time. This multiplex advantage, along with design simplicity, has allowed construction of instruments with 50% transmission and up to a 10^4-fold improvement in detection efficiency.

There are other performance advantages that make the TOF analyzer the preferred choice, especially for static SIMS imaging. It is now possible to produce a Ga^+ ion pulse of less than 1 ns in duration, while maintaining a probe size of 50−100 nm. For example, an ion of mass 100 Da traveling with a kinetic energy of 2 keV through 4 m has a flight time of ~60 μs. Since the flight times of molecular ions can be determined to a precision of better than 200 ps using time-to-digital converter, time resolution of better than 1 part in 300 000 is easily achievable.

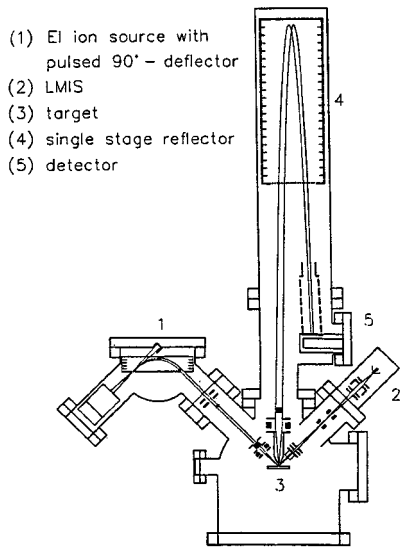

Figure 2. Schematic drawing of the Münster TOF-SIMS III instrument. (Reprinted with permission from ref 8. Copyright 1991 American Vacuum Society.)

The energy spread of sputtered molecular ions is a few electronvolts. This energy distribution causes the major uncertainty in the mass determination as is evident from eq 1. Two strategies are currently being used to compensate for this energy spread. In the first case, the ions are reflected at the end of the flight tube so that the faster ions have a longer flight path than the slower ions. If everything is adjusted correctly, this "reflectron" geometry compensates for the energy spread so that mass resolutions of greater than 1 part in 10 000 are feasible with no loss in spectrometer transmission. Benninghoven and coworkers have pioneered the development of a high-performance system of this type and others have been reported.[54] A diagram of the instrumental setup is shown in Figure 2.[8] A second type of device using three electric sectors to focus ions of slightly different energy, but identical mass, to the detector position has also gained popularity. The specifications of the "TRIFT" analyzer are similar to the reflectron,[26] although the TRIFT has the added advantage of functioning as an ion microscope as well as a microprobe. Both types of designs are now commercially available.

The last type of analyzer utilized in much of the research presented in this review is the double focusing magnetic sector. This analyzer has been introduced to mass spectral imaging experiments by the popular CAMECA series of ion microprobe and microscope analyzers. These analyzers provide high transmission by extraction of secondary ions at very high fields. In addition, high mass resolution is achieved by the use of apertures at various ion beam crossover points along the instrument axis. Perhaps the most appealing aspect of this machine is its ability to acquire ion microscope-type images with a lateral resolution of about 1 μm. The major disadvantage of this instrument is that typically only one mass at a time is amenable to detection, but recent advances have increased detection to four masses at one time.[55] However, it is of interest that the Levi-Setti group has elected to incorporate a magnetic sector into their high-resolution microprobe, previously equipped with a quadrupole analyzer. When coupled with their home-built Ga^+ ion LMIG, this new design is providing lateral resolution of less than 50 nm, perhaps the best value reported yet.[27]

In summary, quadrupole analyzers are giving way to TOF and magnetic sector detectors. The TOF analyzer is best suited to static SIMS imaging because of its quasi-parallel mass detection configuration and high transmission. It is not particularly suited to dynamic SIMS experiments since the pulsed nature of the primary ion implies that the beam dose will be low. The magnetic sector type machines are found exclusively in dynamic SIMS applications where the primary beam is not pulsed and one mass at a time can be imaged.

C. Postionization and Sensitivity Enhancement

Mass spectral imaging requires the effective creation of secondary ions. As noted earlier, and by other authors,[8,56] the number of molecules available for analysis becomes vanishingly small as the pixel size approaches the size of the ion beam probe. This problem is particularly acute for static SIMS imaging where surface damage limits the number of molecules that are desorbed from a given area. There are only 10^6-10^7 molecules/micron^2, for example. It is also limiting in dynamic SIMS experiments where the number of atoms in a specific volume element define the ultimate sensitivity. Acquisition of the highest quality images requires the highest possible ionization efficiency of desorbed atoms and molecules.

One approach to enhancing the ionization efficiency is to use laser radiation to photoionize the desorbed flux above the sample surface.[32] This approach has a number of advantages including the fact that ionization is decoupled from desorption. Therefore, the ionization probability is independent of the electronic properties of the surface.

Many laser ionization schemes have been employed to maximize the number of ions. The first studies employed multiphoton resonant ionization (MPRI), which involves the combination of two or more photons of specific wavelengths that match electronic absorption frequencies of the neutral atoms or molecules.[12,57] The laser beam is directed close to but above the ion bombarded surface so as to intercept the desorbed flux of neutral species. The laser power is increased to saturate the electronic transitions with the hope of achieving 100% ionization efficiency. A second strategy involves the use of nonresonant ionization with one or more high-energy photons to nonselectively ionize the neutral flux.[58,59] This method is perhaps more generally applicable but requires tightly focused laser beams to achieve adequate power density. As a consequence, the spatial overlap between the photon field and the sputtered neutral flux is greatly reduced when compared to the use of MPRI methods.

Recently, ultrashort pulsed lasers have been applied to postionization experiments.[60,61] These schemes have yielded the best results for molecular photoionization studies since pulses of <500 fs appear to cause less photofragmentation than nanosecond pulses.

Another major advantage involves the fact that these lasers can be pulsed at 1000 Hz instead of the more traditional 10 Hz repetition rate. This has significant implications for imaging experiments since at least 10 000 pixels are typically required to create a single image. Assuming one laser shot for each pixel, the acquisition time is reduced from 1000 s to only 10 s. Several examples of how the above laser ionization schemes have been utilized with imaging SIMS applications are shown in section VI.

Electron-beam postionization has also been utilized to enhance ionization efficiency. Direct ionization, by an electron beam directed through the sputtered flux[62] or by the use of a low-pressure plasma,[63,64] has been accomplished and configured for imaging experiments. The sensitivity of these measurements is compared in terms of the useful yield, defined as the ratio of detected ions to sputtered atoms. Useful yields of 10^{-5} are typical for electrons, compared to 10^{-2} for laser postionization, although improvements are forthcoming.

Accelerator mass spectrometry has been coupled to an Ga^+ LMIG to allow imaging of ^{14}C-labeled tracers in sections of biological tissue.[65] This is an interesting approach to sensitivity enhancement whereby positive secondary ions are accelerated to 2 MeV of kinetic energy, and molecular ions are broken down into their atomic constituents, stripped of their electrons, and detected by a QMA as $^{14}C^{3+}$. Initial measurements have been able to resolve ^{14}C-labeled neurotransmitters with about one micron spatial resolution.[66]

D. Quantitative Analysis

Quantitative analysis of chemical components is a difficult task for imaging SIMS. A review of this subject has been published by Morrison and coworkers.[67] The difficulty in quantitation arises because signal intensity is a function of the chemical makeup of the matrix, sample topography, matrix−primary ion beam interactions (degree of erosion), instrumental transmission and detector response.[67] To further complicate matters, some of the above factors are dependent upon one another.

Two approaches are often used to quantify SIMS data: relative sensitivity factors (RSFs) and standards of known concentration. Quantitative SIMS analysis most commonly employs RSFs. The RSFs are a ratio of the intensity of the analyte to the intensity of a reference species of known concentration for a particular matrix. The reference species must be chemically similar to the analyte. Another approach uses standards of known concentrations to develop calibration curves. However, good standards are not always readily available, especially for biological samples, and are often difficult to prepare. So, methods such as standard additions by ion implantation must be employed. Of course, instrumental parameters influence sputtered ion intensity, so oftentimes data from one instrument cannot be used to quantify data for another type of instrument, due to differences in the mass analyzer, primary ion beam, or detector.

Quantitative imaging of biological samples by dynamic SIMS is particularly challenging. Fragu and co-workers have used RSFs to yield relative quantitative information about halogens and Ca using native ^{12}C as the internal standard.[68] Standard calibration curves were constructed using samples of methyl methacrylate resin spiked with either halogen methacrylate or Ca octoate. Their results for biological soft tissues, using the resin-based calibration curves, seem to match data obtained from other methods quite well. However, the authors note that a large number of measurements must be made to achieve statistical significance.

Gillen and Hues applied a quantitative approach to static SIMS analyses of doped gelatin films, a model soft tissue matrix.[69] A variety of biomolecules were investigated including acetylcholine, cocaine, epinephrine, and benzalkonium bromide. Detection limits were as low as 1 ppm. Yet, the curves were nonlinear for organic salts, showing saturation of signal at the highest concentrations. This approach is just one step toward quantitation using static SIMS. Because the signal intensity per pixel in static SIMS is typically far lower than the intensity in dynamic SIMS, quantitation is more difficult.

III. Imaging of Inorganic Materials

The overwhelming diversity of inorganic materials, as well as their complex chemical composition, presents fascinating opportunities for imaging SIMS experiments. The element-specific nature of the measurements for materials applications includes an ability to differentiate between isotopes for diffusion studies, an ability to determine the spatial distribution of components on a small scale in two or three dimensions, and sensitivity to all elements including H and trace analysis capabilities. Many applications in this area tend toward the characterization of materials used in applications where failure would jeopardize human lives, such as in nuclear reactors. Grasserbauer has reviewed MS studies of these types of samples through 1992.[70]

A. Metals

1. Metals, Alloys, and Silver Halides

The properties of metals and alloys are governed by the distribution of major and trace elemental components segregated in phases, along grain boundaries, as precipitates, or homogeneously distributed throughout the material. Imaging dynamic SIMS cannot only probe the elemental distribution in two-dimensions, but also in three dimensions, creating a 3-D picture of sample chemistry.

Three-dimensional SIMS has been used to characterize compacting processes for refractory metals (W and Mo) in order to develop a sintering process. The authors report the purity of the metals as 99.9999%.[71] Imaging SIMS experiments show that the distribution of trace impurities in electron-beam melted Mo exhibit grain boundary segregation of H, C, and O. In contrast, sintering of Mo results in similar contaminant levels but they are homogeneously distributed, which is more desirable. These results are significant because nonimaging analytical techniques

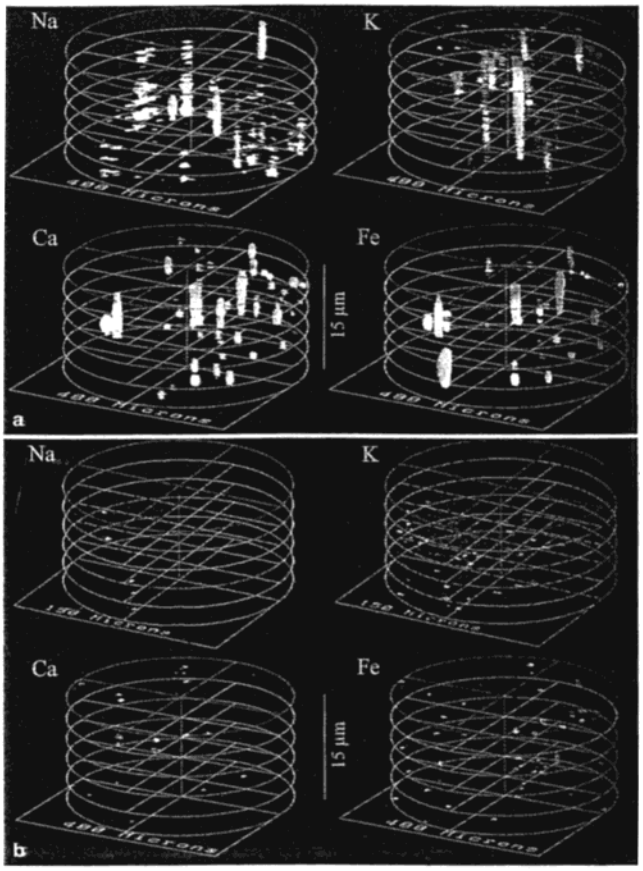

Figure 3. 3D-SIMS images of (a) 99.9999% purity tungsten produced by hot pressing and (b) 99.9999% purity tungsten produced by an optimized sintering process. (Reprinted with permission from ref 71. Copyright 1995 Springer Verlag.)

could not have determined a difference between the two Mo samples. Hot pressing of W results in large precipitates (2−20 μm) of O, C, H, Na, K, Ca, and Fe, some of which are shown in Figure 3.[71] Sintering of W, on the other hand, results in a product with much less contamination and very small or no precipitate formation. The sintering process has been shown to yield superior material compared to hot pressing and electron-beam melting. The lateral resolution is 1−2 μm and the depth resolution is less than 10 nm for these experiments.

High-speed steel (HSS) properties and behavior are influenced by the number and distribution of impurities such as oxides, nitrides, carbides, sulfides, and gas bubbles, which can weaken the steel. Grasserbauer and co-workers investigated impurities in HSS using imaging SIMS.[72] Ring-shaped precipitates of B, Al, and Ti are clearly evident as well as smaller S-containing precipitates. In addition, each of the three phases show some segregation of components such as C, V, and Cr. Two ion guns, Cs^+ and O_2^+, were used separately to garner more information from the steel than could be obtained using only one primary ion source.

Fusion reactors are constructed from V−Cr−Ti alloys, so the welds used for these alloys must be especially robust. Images of minor and trace element distributions in a weld were correlated with the weld properties in order to engineer optimum weld materials.[73] Since V reacts with H, O, and N, SIMS measurements can predict the possibility of weld failure from the presence of these elements before the materials are put to use. Comparison of results to ion implant standards for N, O, and S allowed for quantitation of these elements. Gas tungsten arc welds caused C- and O-rich particles at the edges of V grains, which could weaken the metal and cause weld failure. Electron-beam welding caused segregation of O and S at the V grain boundaries and a uniform distribution of P.

Electronic power device assemblies are soldered with Pb−Sn−Ag and Pb−Sn alloys. Therefore, cracks that develop in solder joints, from thermal cycling, in these materials are a possible cause of device failure. X-ray photoelectron spectroscopy (XPS), three-dimensional SIMS, scanning electron microscopy (SEM), and electron probe microanalysis (EDAX) were used to characterize the fatigue failure of Pb−Sn−Ag solder joints during plastic deformation.[74] SIMS images showed Sn depletion and Pb enrichment around some cracks of mechanically stressed joints. Since the Pb-rich phase is mechanically weaker, it could be one source of joint failure.

Photographic film is composed of silver halide crystals embedded in a gelatin matrix. There are many silver halide crystal formations, the composition and distribution of which affect the film quality. Levi-Setti and co-workers have used SIMS to characterize the location of the halide content of these microcrystals and ion etching to reveal the interior structures.[75,76] Similar work has been reported by Verlinden et al.[77] Holographic interference fringes were imaged with very high spatial resolution in an emulsion using SIMS.[76] The coincident distribution of Ag and Br in the holographic fringes is shown in Figure 4. The line separation is 300 nm, which is consistent with the red color of the hologram. Such high lateral resolution indicates the potential of imaging SIMS for application where chemical heterogeneity exists on a small scale. The researchers also investigated the fibrillar nature of the gelatin matrix.

2. Diffusion and Corrosion

The study of solid state diffusion involves the exposure of a sample to a labeled species (e.g., ^{18}O) followed by imaging of the sample to obtain lateral and/or depth distribution of the label. A profile of the labeled species indicates where diffusion has taken place and the mechanism of the diffusion process. The formation of protective oxides on metals and alloys via diffusion has been the focus of many SIMS investigations. Interfaces and grain boundaries are important, yet are difficult regions to characterize by methods other than SIMS. The oxides can form protective layers on metallic surfaces, which can be damaged by defects allowing attack of corrosive species.

Prescott et al. have investigated the growth of protective Al_2O_3 scale on FeAl and NiAl.[78,79] The nature and direction of the diffusing species that form the surface coating are currently unclear. Zirconium-doped β-NiAl has potential for use in high-tempera-

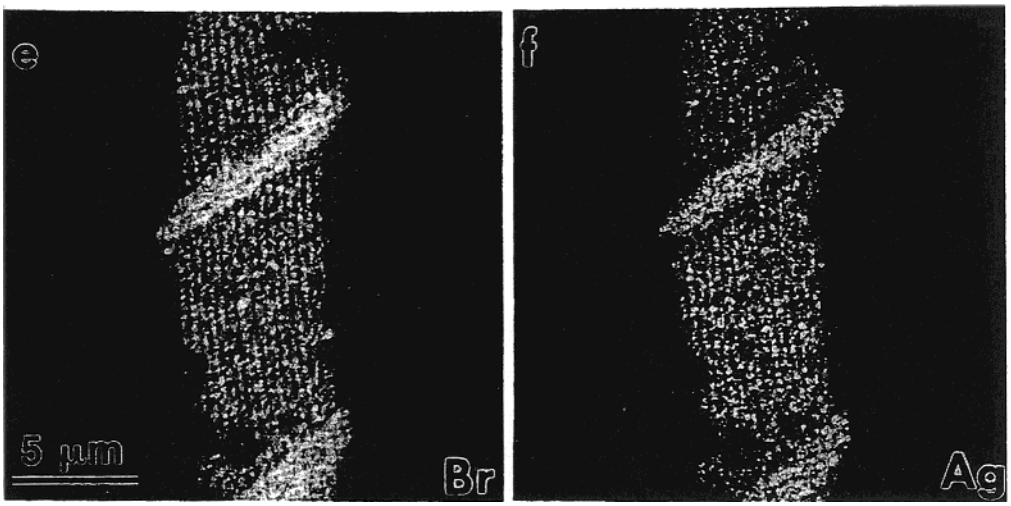

Figure 4. Analysis of a cross section through an Ilford Holofilm (e) Br^- and (f) Ag^+ maps of a holographic interference fringes (vertical stripes). The bright diagonal features are a preparation artifact. (Reprinted with permission from ref 76. Copyright 1995 IS&T.)

ture cooling systems and structural applications, so understanding the growth of Al_2O_3 scale, which leads to corrosion resistance, is of fundamental importance. Samples were first exposed to ^{16}O, and then ^{18}O and images at various depths through the oxide layer were obtained. The ^{18}O is found on the outer surfaces of the scale, but not within the scale or at the scale−alloy interface. The data, combined with other information, suggest that oxidation takes place by outward Al diffusion. After the initial layer of Al_2O_3 is formed, it appears that further outward Al diffusion is accompanied by inward O diffusion along the grain boundaries. SIMS data show ^{18}O at the outer surface of the Al_2O_3 layer, at the grain boundaries, and at the NiAl−scale interface. Results also indicate that Zr diffuses outward with Al, forming oxides at both the scale−NiAl interface and the outer surface of the scale. Understanding the formation mechanism of protective scales on alloys should allow the engineering of alloys with protective coatings which possess desired characteristics.

Alumina scale also protects FeCrAl-based alloys, which are used as high-temperature construction materials in corrosive environments. It has been shown that the Y dopant concentration has a beneficial effect on the growth rate of the scale.[80] For Y concentrations between 0.17% and 0.7%, SIMS data show that oxygen diffusion occurs on oxide grain boundaries. However, alloys with 0.02% Y show signs of upward Al cation diffusion and less downward oxygen diffusion. Therefore, it is proposed that the Y concentration must be higher than 0.02% to inhibit Al diffusion, suggesting that the presence of Y in grain boundaries may change the diffusion pathways of Al.

Corrosion of Cr can also be inhibited by the formation of an oxide layer on its surface. However, spallation of the protective oxide is thought to result from contaminants in the Cr. Grasserbauer and coworkers investigated the formation of the oxide using 3-D SIMS.[81] Sequential reaction of Cr with ^{16}O and ^{18}O results in a layer of $Cr^{18}O$ atop a layer of $Cr^{16}O$. These data imply that O does not diffuse to the oxide−metal surface, but that Cr diffuses upward. Because N and Cl are not soluble in chromium oxide, they were found to diffuse through grain boundaries and form a layer at the oxide−metal interface. The accumulation of N and Cl reduces adhesion of the oxide and causes spalling.

In the examples above, oxide layers served to protect the underlying material; however, growth of oxide on uranium monocarbide (UC) has a deleterious effect. Initial stages of oxidation of UC are not well understood on a microscopic scale. Asuvathraman et al. used SIMS to investigate the very thin oxide layer on UC.[82] Uranium monocarbide is a fuel for fast breeder reactors, but suffers from rapid reaction with oxygen and H_2O. Using a combination of XPS, X-ray diffraction (XRD) and SIMS, the researchers identified a top layer of adsorbed moisture and oxygen contamination. Below this was a layer of uranium oxide, uranium hydroxide, free oxygen and grain-bound oxide, and beneath this, bulk UC. The results indicate that extreme care must be taken to avoid this detrimental atmospheric contamination.

Corrosion of tinplate is a great concern for the food industry. Three-dimensional SIMS investigations have shown that the processing step of tinplate is probably the primary cause of the failure.[83,84] Tinplate is applied to steel by electroplating Sn on rolled steel, and then by reflowing the Sn to ensure proper adhesion and iron−tin alloy formation. Imaging SIMS reveals inhomogeneous Sn coverage, which causes corrosion. The authors propose that the inhomogeneity is a result of the rolling process because there is little or no Sn on the raised ridges between the rolling grooves. The patches of exposed Fe can corrode.[84] Figure 5 displays 3-D images of C, O, Fe, Sn, FeSn, and FeO from tinplated steel, which exhibit a large amount of pitting.[83] Inhomogeneities can easily be seen in all images, particularly where Fe, O, and FeO extend up to the surface. Furthermore, the FeSn alloy is not continuous. It clearly does not form a protective barrier, as it does in steel that exhibits no pitting.

High-strength steels undergo delayed fracture caused by hydrogen trapping and reaction. Researchers have simulated conditions of delayed fracture to

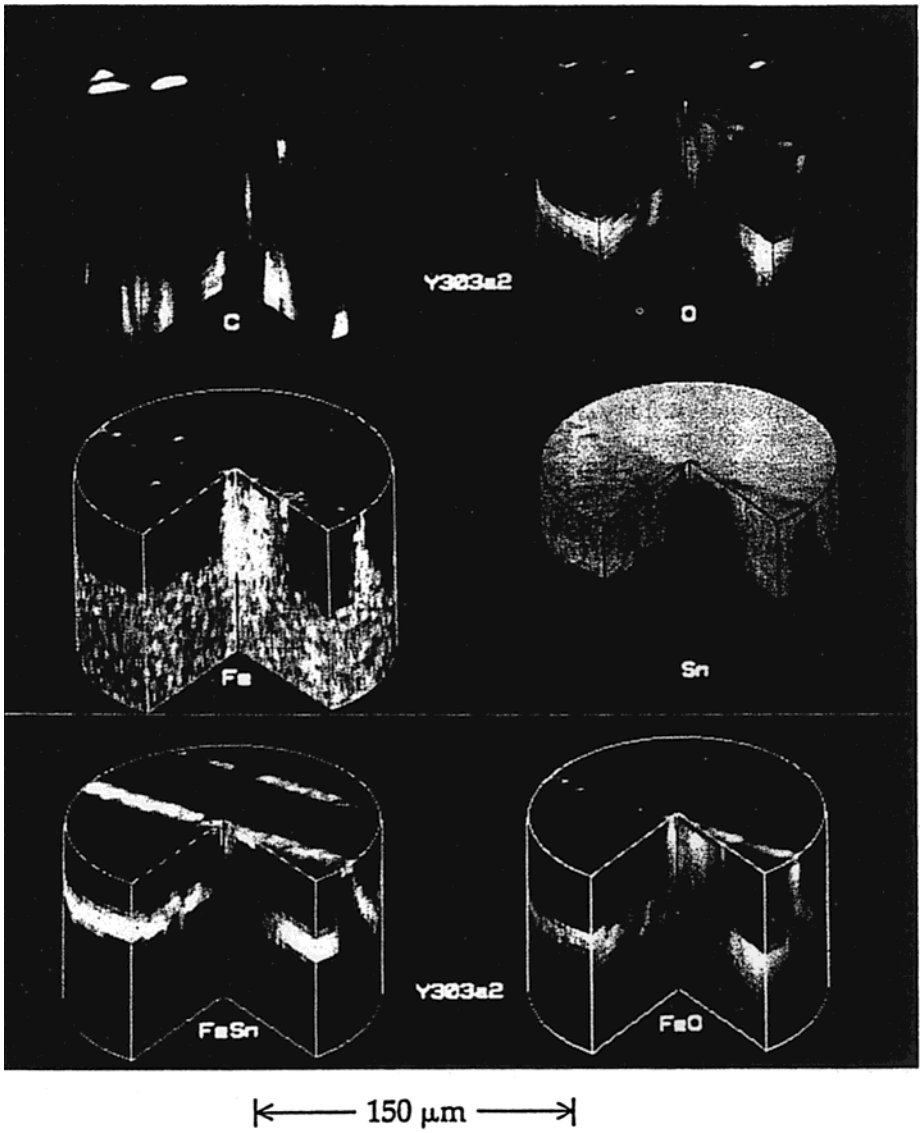

Figure 5. Pseudo three-dimensional SIMS image volumes through the surface of a tinplate exhibiting 60% pitting on the surface. Eight-bit intensities are represented. The imaging field is 150 μm. (Reprinted with permission from ref 83. Copyright 1994 John Wiley and Sons.)

determine the location of hydrogen-trapping sites in the hope that insight into the mechanism of delayed fracture will allow them to make more fracture-resistant steels.[85] Steel was first stressed, and then dipped in D_2O and NH_4SCN to label H-trapping sites introduced as a result of the delayed fracture test with deuterium. Imaging SIMS reveals that there is H and D present on grain boundaries, in nonmetallic inclusions and in the segregation band of P. Trapping site information is provided with little difficulty using SIMS, despite the low atomic number of H. In addition, other methods of determining hydrogen-trapping sites, such as tritium autoradiography, are more expensive and time consuming because of the use of a radioactive element.

The active sites for oxygen reduction on solid fuel cell electrode materials have been investigated using SIMS.[86] For the most efficient fuel cell, it is important to have an optimal cathode−electrolyte interface. In this case, the electrolyte is yttria-stabilized zirconia (YSZ) and the cathode is strontium-doped lanthanum (LSM). The determination of the location of active sites at the O_2/LSM/YSZ interface can provide information about the reaction mechanism and optimum electrode structure. An LSM mesh on a YSZ disk was exposed to ^{18}O under cathodic polarization. A high concentration of ^{18}O is seen on the LSM electrode in SIMS images. After etching the electrode with HCl to remove the LSM grid, ^{18}O spots were also localized at the previously existing LSM/YSZ interface. The authors propose that O diffuses through the solid LSM electrode to the active sites at the LSM/YSZ interface.

Nickel-rich superalloys, such as Alloy 800, are potential materials for use in coolant circuits of nuclear power stations. However, they are susceptible to corrosion in dilute alkaline environments. The corrosion of Alloy 800 has been characterized using 2-D and 3-D SIMS imaging.[87] Hydration of the oxide layer was tracked with D from D_2O exposure. The researchers find that the oxide film on Alloy 800 is not homogeneous in nature. FeO is only found near the outermost oxide layer, and NiO is found throughout the entire oxide layer. CrO, on the other hand, is

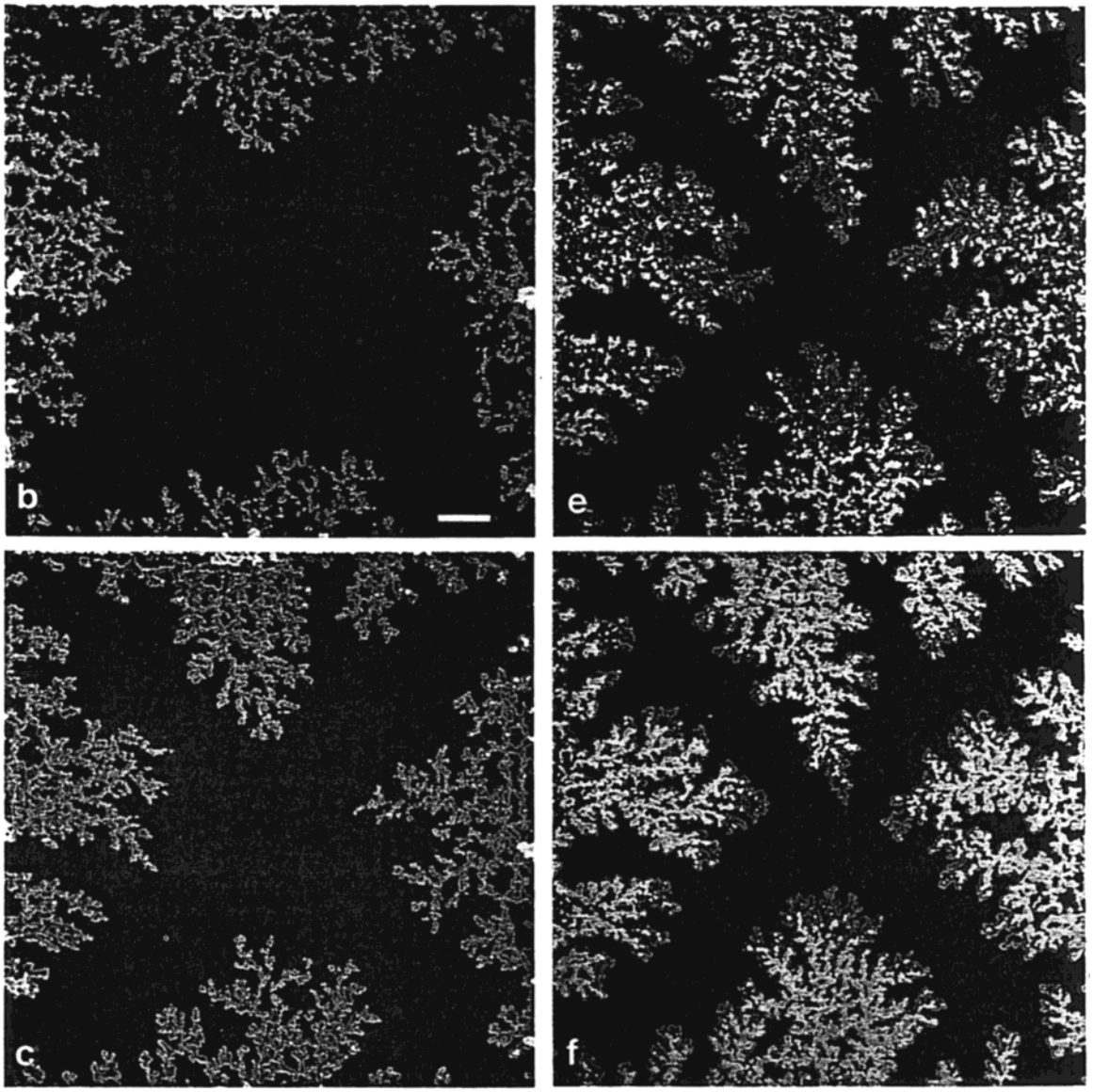

Figure 6. Secondary Ga^+ ion maps showing the early stages of growth of an oxide layer on a liquid gallium surface. (b)−(f) are snapshots of the oxide growth within the window, scale bar = 5 μm. The pressure (Torr) in the specimen chamber, the cumulative oxygen dose (O_2/cm^2), and the fractional area covered by each stage are: (b) 1×10^{-7}, 3.2×10^{16}, 11%; (c) 1×10^{-7}, 7.5×10^{16}, 21%; (e) 2×10^{-7}, 1.7×10^{17}, 37%; (f) 2×10^{-7}, 2.8×10^{17}, 43%. (Reprinted with permission from ref 88. Copyright 1989 Scanning Microscopy International.)

found throughout and below the hydrated-oxide layer of FeO and NiO. CrO is also found as precipitates below the oxide film. Sodium atoms migrate along grain boundaries and is therefore found as threads extending to the oxide layer. The behavior described above is not characteristic of all Ni-rich superalloys since different results are obtained from Alloy 600 after identical chemical treatment.

A twist on the typical method of diffusion characterization is to damage a surface with an ion beam, and then to observe that surface via imaging SIMS to monitor the growth or movement of chemical species on the damaged area. This method was used to study the dendritic growth of oxide on liquid Ga exposed to O_2 in a vacuum.[88,89] The oxide growth begins from the existing oxide layer and grows toward the clean Ga surface. The initial stages of growth, which can be seen in Figure 6,[88] agree with computer simulations based upon 2-D diffusion-limited aggregation (DLA). In situ analysis allows the growth of dendritic oxide on Ga to be characterized for the first time.

Benninghoven and co-workers recently applied similar techniques to study room temperature polymer diffusion on Ag in a vacuum.[90] Four polymers, polystyrene (PS), poly(dimethylsiloxane) (PDMS), poly(methyl methacrylate) (PMMA), and Krytox, were deposited on etched Ag substrates. The primary ion beam was then used to damage a section of the surface. Images of this damaged area were subsequently acquired as a function of time as can be seen in Figure 7.[90] Krytox and PDMS show considerable surface diffusion into the damaged area whereas PMMA and PS show no diffusion. Because the images of diffusion were obtained as a function of time and position, diffusion coefficients could be calculated and were found to be 1.9×10^{-7} cm^2/s for PDMS D17, an oligomer with 17 repeat units.

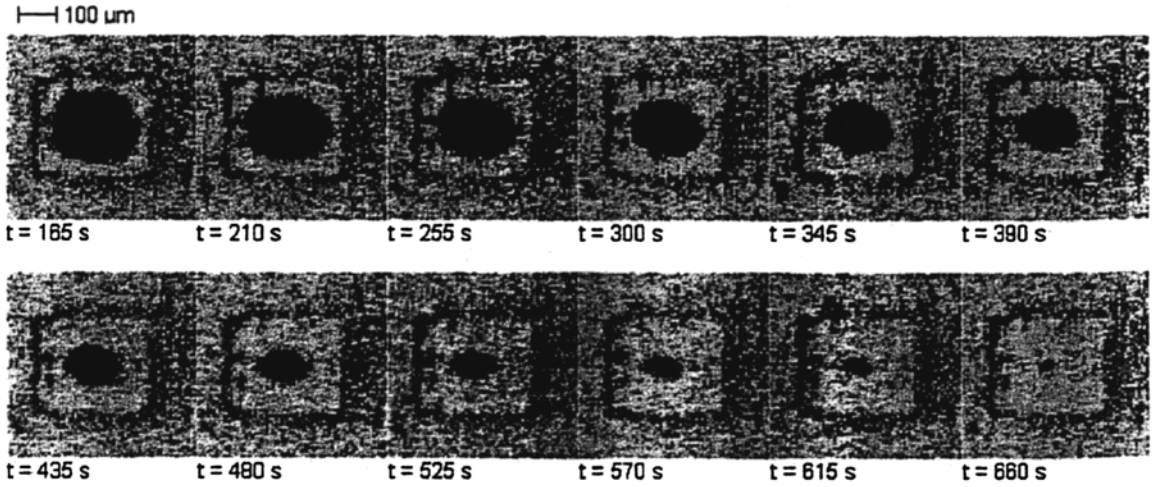

Figure 7. Lateral distribution of $(M + Ag)^+$ emission from a PDMS D17 monolayer on Ag as a function of time. Prebombardment: 240 × 240 μm^2, PIDD: 10^{15} cm^{-2}; imaging 480 × 480 μm^2, PIDD: 2×10^9 cm^{-2}. (Reprinted with permission from ref 90. Copyright 1998 Elsevier Science.)

B. Ceramics, Oxides, and Nitrides

1. Ceramics

Ceramics have complex microstructures, and multiphases, and often contain light elements and trace concentrations. Imaging SIMS can provide useful information about the composition of ceramics. Levi-Setti and co-workers have recently reviewed several studies of ceramics carried out using imaging SIMS.[27]

Soni et al. characterized impurity and additive distributions in a $YBa_2Cu_3O_{7-x}$ superconductor.[91] As shown in Figure 8, Na and Cl are found in high concentrations in the grain boundaries. These same grain boundaries are also deficient in Cu and O. Obviously, the grain boundaries are not superconducting, because they do not contain Cu and O and they deteriorate the superconductor performance. Levi-Setti and co-workers also determined that $YBa_2Cu_3O_{7-x}$ derived from $BaCO_3$ shows detrimental C contamination at grain boundaries compared to superconductor samples derived from B_3N_2.[92] Gillen and co-workers have also characterized a $YBa_2Cu_3O_{7-x}$ superconductor using SIMS.[93] Fluorine was found as a contaminant that diffused in one plane of the crystal. The authors propose that the sources of fluorine are O-rings used in a processing furnace. The substitution of F for O is not necessarily detrimental since it may increase the transition temperature (T_c).

Polycrystalline alumina (Al_2O_3) is a commonly used ceramic. Increasing creep resistance of alumina by doping the material with Y, and possibly La, is often desired. Levi-Setti and co-workers investigated the localization of Y and La in alumina.[94] Grain boundary diffusion is believed to be inhibited by Y at grain boundaries which limits creep. Precipitates of Y were also found, which is another potential mechanism of creep inhibition. Similar segregation patterns are exhibited by La, which could also hold promise for increasing creep resistance.

Magnesia (MgO) is used as a sintering aid for alumina (Al_2O_3) to produce a material used in commercial lighting applications. However, analytical methods other than SIMS have not been able to definitively determine the distribution and role of Mg in polycrystalline Al_2O_3. Segregation of both Mg and Ca at grain boundaries in alumina is shown in Figure 9.[95] The concentration of Ca in the bulk is less than 10 ppm. These elements are still seen in the alumina crystals, although at 75−100 times less intensity than at the grain boundaries. From these results, the authors propose that the role of Mg is to reduce the mobility of the grain boundary and thereby affect grain growth producing a product suitable for lighting application.

2. Catalysts

The strength of chemical imaging analysis may be greatest where the heterogeneity of chemical species has an effect on the function of a material. Catalysts typically fall into this category. Fluid cracking catalyst microspheres are made up of zeolite−catalyst phases and aluminosilicate−matrix phases. SIMS has been used to characterize the Na content of these microspheres, since Na affects the activity and stability of the catalyst.[96] After simulating the steam conditions to which these microspheres are typically exposed, the authors find that Na migrates from the zeolite to the matrix. At the same time, zeolite debris, indicated by high Si and low Al signals, migrate into the matrix. This migration is believed to be the reason for the degradation of catalyst performance under hydrothermal conditions. Fluid cracking catalysts are frequently poisoned by V, a major contaminant from steel refinery equipment. Chao et al. investigated the use of a Ca-containing clay matrix to scavenge V.[97] SIMS images demonstrate that V is preferentially segregated in the clay phase instead of in the catalyst.

3. Coatings

Coatings of protective films often allow materials to be used in corrosive environments. The integrity of the film determines the degree of protection that it serves. Therefore, methods are needed to characterize the homogeneity of the coating and any reactions the coating has with the underlying material.

Ingo and Padeletti have used SIMS, Auger electron spectroscopy (AES), and XPS to characterize coatings

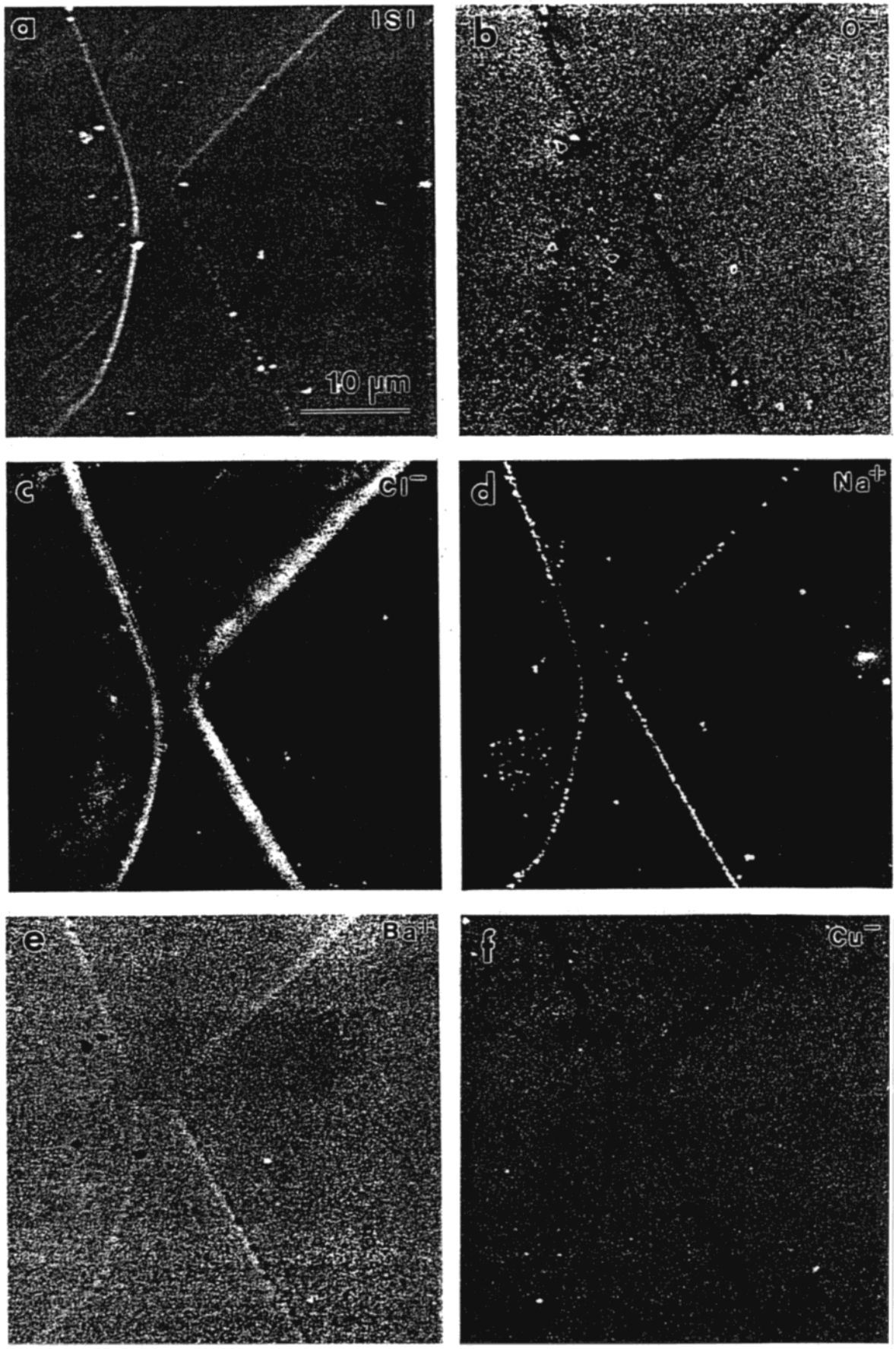

Figure 8. Correlative SIMS maps of a $YBa_2Cu_3O_{7x}$ specimen: (a) ion-induced secondary ion (ISI) image; (b) O^-; (c) Cl^-; (d) Na^+; (e) Ba^+; (f) Cu^-. Impurities such as Na and Cl segregate to the grain boundaries, whereas O and Cu signals show depletion. Absence of Cu^- emission from the grain boundaries is indicative of a loss of superconducting behavior in this region. (Reprinted with permission from ref 91. Copyright 1994 John Wiley and Sons.)

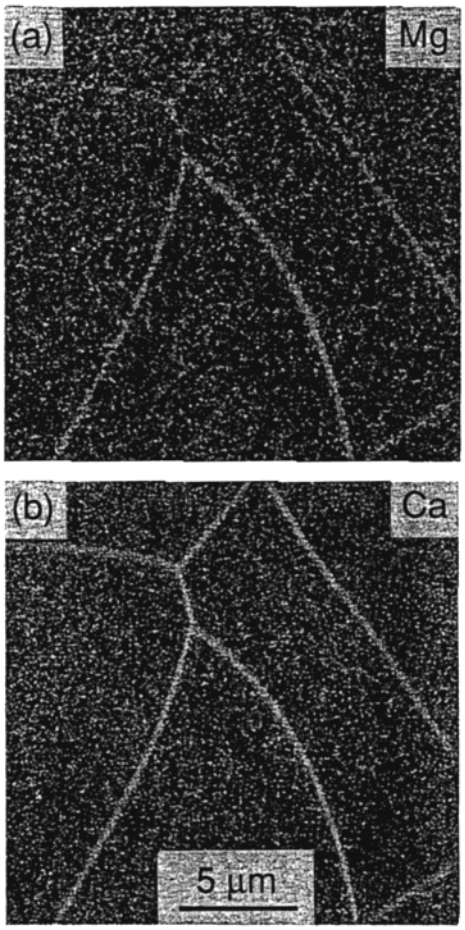

Figure 9. (a) Mg^+ and (b) Ca^+ SIMS maps of polycrystalline Al_2O_3 doped with 250 ppm MgO and sintered at 1800 °C for 18 h followed by cooling at 10 °C/min; brighter features represent higher concentrations. Each image was acquired in 524 s using a 512 × 512 raster and contains no noise signal. Both Mg (dopant) and Ca (impurity) are clearly segregated to the grain boundaries. Small amounts of these elements are present within the grains, corresponding to their solid solubility in alumina at the sintering temperature. On average, grain boundary layers appear to be ~4× (a) and ~3× (b) brighter than the grains. Assuming the segregation width to be two monolayers, segregation ratios (grain boundary/grain concentrations) computed from the digitally recorded SIMS maps are ~100 and 60 for Mg and Ca, respectively. Si was not detected in this sample. (Reprinted with permission from ref 95. Copyright 1995 American Institute of Physics.)

on metallic substrates.[98,99] Boron nitride coatings are used to protect steel because they are electrical insulators and good thermal conductors and are stable. A new method of coating steel with BN was investigated using SIMS and XPS.[98] Boron-doped steel was treated with NH_3 at high temperatures. In low boron content steel, B reacts with NH_3 at the grain boundaries. For steel with higher boron content, BN was seen at grain boundaries and on much of the surface. In addition, rapid migration of Al, Cr, C, and Si at high temperatures formed AlN, CrN, CN, and SiN to be found at grain boundaries. The results indicate that high concentrations of B in steel yield more complete coverage of the surface with BN, suggesting that this new method of BN coating formation may hold promise.

C. Composites

Composite materials are often composed of fibers embedded in a matrix. It is the combination of the properties of the fiber and the matrix that gives composites unique characteristics. Therefore, the reaction of the matrix with the fiber must not degrade the advantageous properties of the combination of materials. In fact, the bonding of the matrix to the fiber is of crucial importance to the performance of a composite. One way to ensure that proper bonding takes place is to use a binding agent on the fiber, which facilitates bonding to the matrix. Imaging SIMS, as in the case of corrosion studies, provides details of the chemistry of phases, grain boundaries, and precipitates.

Changes in composite processing methods are one approach to optimizing this bonding between the fiber and the matrix. The success of processing has been evaluated using SIMS imaging.[100] A low cost, yet high performance material can be made from the incorporation of alumina−silica fibers in an aluminum−magnesium alloy. Four separate composites were made by varying the calcination temperature and following heat treatment. Imaging SIMS shows that Mg from the matrix diffuses into the SiO_2 binder and also precipitates into the matrix when the materials are calcined at 850 °C and air cooled. However, when the calcination temperature is raised to 1200 °C, no reaction was observed between the binder and the fiber. Water quenching treatments at both calcination temperatures result in fiber damage. Following calcination at 850 °C, Si lost from the fibers formed large precipitates in the matrix, and Mg is found to replace the binder layer. After calcination at 1200 °C and water quenching, fiber damage is observed as Si precipitates around the fibers, although the fibers still retain some Si. The reaction of Mg and Al with the SiO_2 binder is not uniform in character. The MgO surrounds the fibers and diffuses into them along with Al. The SIMS images not only indicate fiber damage but also reveal the cause of the damage. A similar paper about this composite system was published elsewhere.[101]

Levi-Setti and co-workers compared EPMA and SIMS for the characterization of three fiber-reinforced composites and stressed that the techniques complement each other.[102] The composites studied in these experiments are well suited to SIMS analysis because they comprise a distribution of light elements. Their experiments were able to unravel the distribution of elements, the identity of phases, and the interfacial reactions in fiber-reinforced composites. A B-doped Ni alloy was selected as a binder around the alumina fibers because of its lower melting point. In this way, heat processing could be used to bond the fibers to the matrix without damaging the fibers during heating. Imaging SIMS reveals that the matrix−fiber interface is enriched in Al, Ni, and B, but not Co and Cr. Since not all elements appear enriched at the interface, the authors conclude the enrichment is not an artifact caused by matrix effects. However, the B enrichment does not exist at all interfaces, which indicates a nonuniformity induced through processing. Due to its low

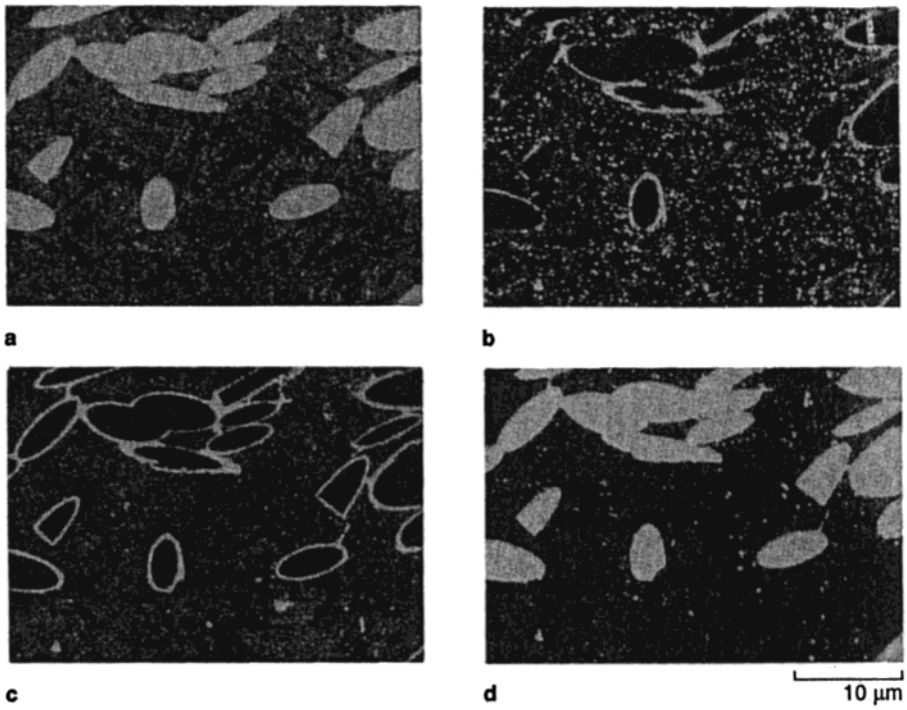

Figure 10. SIMS Maps of a squeeze-cast alumina-fiber-reinforced Al−Si−Mg alloy. (a) Al^+ map. The fiber cross sections appear as bright aluminum-rich ovals. (b) Si^+ map. (c) Mg^+ map. (d) O^- map. (Reprinted with permission from ref 102. Copyright 1993 Minerals, Metals and Materials Society.)

solubility in the alloy, B is also found in precipitates at grain boundaries in the matrix. A more detailed examination of this fiber-reinforced Ni alloy has also been published.[103]

Figure 10 contains SIMS images from a material made by the squeeze infiltration of Al_2O_3 fibers with a SiO_2 binder into a molten Al-based alloy.[102] The distribution of Mg in this material was investigated, because Mg reduces both SiO_2 and Al_2O_3, which weakens the material. The Mg is not found in the Al_2O_3 fibers, but is found in the matrix. In the images, it appears that the fibers contain more Al than the matrix. However, the opposite is actually true. The fibers contain ~40% Al and the matrix contains ~92% Al. The Al signal is enhanced in the fibers because of the presence of O. A third study probed the interface between an aluminum borate ceramic and SiC fibers.[56,102]

D. Semiconductors

Particulate contamination in semiconductor processing is detrimental to device fabrication. As both the sizes of component features and the acceptable contaminant levels decrease, the characterization of these features becomes more difficult. Comparisons of the potential of AES, TOF-SIMS, SEM/EPMA, and XPS to image particulates on Si and determine their size and composition have been made.[104,105] An obvious advantage of static SIMS imaging is the ability to characterize the organic contaminants, as well as the inorganic component. Particles of Al, Al_2O_3, and TiO_2 in a size range from 0.1 to 0.5 μm could all easily be located by imaging SIMS as shown for a set of 0.1 μm particles in Figure 11.[105] However, static SIMS cannot differentiate between a metal and a metal oxide because metal particles typically have a layer

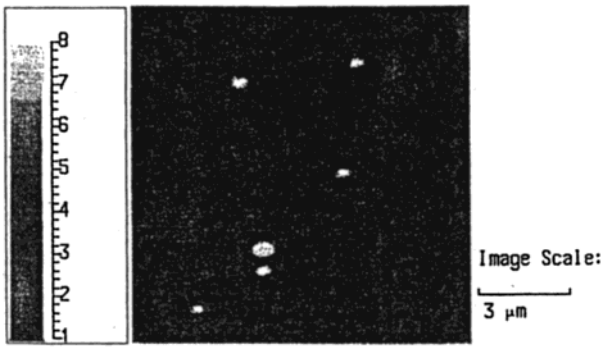

Figure 11. TOF-SIMS total positive ion image from the 0.1 μm Al particle sample. (Reprinted with permission from ref 105. Copyright 1996 American Vacuum Society.)

of metal oxide on the outside. If the metal oxide is thicker than the sampling depth, then static SIMS cannot determine the bulk makeup of the particle. However, depth profiling in the dynamic SIMS regime, which etches through surface layers, can more completely characterize particles.

E. Minerals

The location of chemical species along grain boundaries, as precipitates and in bulk, can have a profound impact on the commercial value of minerals. Coal has been extensively characterized by SIMS to better evaluate the chemistry behind its stability, processing characteristics, and combustion properties. In addition, the chemical distribution of species in samples of extraterrestrial or earthly origin indicates the mechanism of formation and the place and time of origin. Lastly, optimization of mineral processing frequently depends on knowledge of the chemical distribution and the reactions of reagents with ores and minerals.

Coal is a vital fuel resource composed of a heterogeneous distribution of minerals and phases. Particulate matter generation is associated with the distribution of species on the surface of freshly cleaved coal. Gong et al. used XPS, TOF-SIMS and laser ionization mass analysis (LIMA) to characterize the surface of freshly cleaved coal and coal dust.[106] Imaging SIMS has revealed regions of aluminosilicates, clays, and carbonates in one type of coal and has delineated the spatial distribution of trace amounts of Sr, Ba, and Na found on the surface. In another experiment, Gong et al. investigated the inorganic nitrogen in coal, a source of NO_x pollution and a factor in the stability of coal, using XPS and TOF-SIMS analysis.[107] Nitrogen was found in an ammonium form in the clay-rich areas of middle rank coal, suggesting that the presence of ammonium is not unique to the age of coalification.

Imaging TOF-SIMS has been performed on pyrite-containing coal to determine the distribution of those elements which affect the processing of coal and the impact coal has on the environment after combustion.[108] C_2H and CH ions define the organic phase, although these same species are found on pyrite grains, probably due to physisorption. A pyrite phase is defined by the distribution of Fe and is also found to contain Ni, Cu, and Cl, in agreement with other studies. Clay phases are indicated by the presence of Si with one clay phase also containing Li and Al and another containing Ca and Mg. In spite of the low concentrations, imaging SIMS is able to characterize the elemental distribution of heterogeneous coal.

Low-temperature oxidation of coal was the focus of two studies by Martin and co-workers,[109,110] because oxidation degrades the metallurgical properties of coal. They oxidized coal with $^{18}O_2$ to differentiate between preexisting ($^{16}O_2$) and new sites of oxygen reactions. Sequential derivatization was used to extend the amount of information obtained through conventional SIMS analysis by identifying functional groups based on their reactivities with specific probes. For example, reaction with CD_3I converts the OH on the surface to methyl ethers or acetates, and acidic hydrogens are indicated by Rb deposits, after reaction with RbOH.

Meteorite chondrules (spherical or oval regions) are found in primitive meteorites. Processes that form these structures have been the subject of speculation. Levi-Setti and co-workers have imaged the edge of a large chondrule.[111] They find O, Al, Na, Mg, and Fe at the edge of one chondrule. Unexpectedly, the Fe distribution varies from one chondrule to another, which may indicate that chondrules in one meteorite can have different histories of formation. Interplanetary dust from the stratosphere was characterized by Stephan et al.[112] Analysis of the chemical distribution of such particles indicated the origin of the particle (terrestrial or extraterrestrial) and the nature of contamination from the stratosphere. Mathez et al. recently studied a carbonaceous film on the crack surfaces of a pyroxene grain from a gabbro xenolith in basalt by imaging TOF-SIMS.[113] They found that this film also contains Ni and Cu, possibly as organometallics. In addition, islands of Na, Ca, Si, and Al oxide are found under the carbon layer. The authors believe that the islands result from a reaction with volcanic gases or acidic waters, probably before the formation of the carbonaceous layer.

Reactions of minerals with chemicals during mineral processing and in water reservoirs have also been studied using SIMS. Mineral precipitation in reservoirs was characterized using sandstone exposed to $H_2{}^{18}O$.[114] The fluid−rock interaction was then determined by examining precipitates containing ^{18}O. Oxidation products resulting from processing were differentiated from native oxides[115] based on ^{18}O content. This experiment shows that the stain on the feldspar is due to iron oxide, which could be a source of a permeability change in reservoir rock. Similar experiments were previously reviewed in a related paper.[116]

Mineral flotation is a separation process whereby valuable ore is floated up on bubbles of ore-specific float agents (the collector) leaving the other rock components behind. The interaction of dialkyl phosphinates with galena was investigated by imaging TOF-SIMS.[117,118] SIMS is especially well suited to this analysis given the very low coverage of the agent on the galena surfaces. Even with the small amount present (monolayer to submonolayer), a distribution of the molecular ion of diisobutyl dithiophosphinate could be determined.[117] The images suggest that there is a nonuniform distribution of the floating agent on the crystal surface, with preferential adsorption to O-rich areas.[118]

Magnesium silicates are common contaminants in ore after separation of metal sulfides by flotation. The interaction of pyroxene, a magnesium sulfide, and isobutylethoxycarbonyl thionocarbamate (IBECTC), a collector, was investigated by XPS and imaging TOF-SIMS.[119] When pyroxene is treated with IBECTC, the collector-associated signal (CN) is not seen on the surface of the pyroxene crystals. When Cu^{2+}, a common contaminant, is allowed to react with pyroxene crystals, SIMS images show Cu to be present on their surfaces. In the presence of both Cu and IBECTC, images show both Cu and CN on the surfaces of the pyroxene crystals. The authors propose that the collector binds to Cu sites on the pyroxene surfaces. Although this is a potential mechanism of metal sulfide ore contamination, it is noted that the presence of the collector on the surfaces of the crystals does not necessarily mean the crystals will float.

In summary, imaging SIMS offers many advantages when characterizing materials. Almost all elements and isotopes can be detected, which is especially important in cases where light elements, like H, are of interest, and in the study of corrosion using isotopically labeled species to establish a time scale of events. For composites, effects of processing conditions can be monitored by observing the diffusion of chemicals through imaging SIMS. The collection of impurities at grain boundaries can indicate reasons for material failure. Furthermore, 3-D SIMS images depict the chemical distribution throughout a material and provide a comprehensive chemical

distribution. Currently, imaging SIMS information is limited by the influence of the matrix on ion yields, which can affect concentration calculations, and different sputtering rates for different species which affect 3-D profiles.

IV. Imaging of Organic Materials

The capability to directly obtain the distribution of organic molecules with high surface specificity is an exceptional quality of imaging static SIMS analysis. Polymers are widely used, but the characterization of their distribution on a surface can be difficult to obtain for chemically similar molecules. Static SIMS imaging of polymers, and organic molecules on polymer surfaces, is one application that has great potential, but has seen relatively little use. Furthermore, imaging SIMS analysis of microelectronic devices patterned with thin organic films is relatively easy to do and will be important as technology searches for new device fabrications.

A. Polymers

Polymers have been extensively studied using SIMS; however, imaging is not typically used for their characterization since the chemical distributions of the polymer tend to be homogeneous.[120,121] Copolymer blends, on the other hand, exhibit phase segregation and domain formation. Imaging of these domains can indicate which preparation methods or relative concentrations of each type of polymer are desired for a particular application. Weng et al. chemically mapped a slowly cooled and a quenched sample of an ethylene−tetrafluoroethylene (ETFE)/poly(methyl methacrylate) (PMMA) copolymer.[122] Imaging TOF-SIMS of two groups of ions, O and OH (indicative of PMMA) and F (indicative of ETFE), exhibits differences in miscibility between the differently prepared samples. Slowly cooled samples consist of ETFE particles dispersed in a PMMA matrix with only small areas of both PMMA and ETFE. On the other hand, quenched samples still have the same particle distribution, but contain a large amount of coexisting PMMA and ETFE, which influences the polymer properties.

Dias and Galuska examined phase segregation and colocalization of metals within different polymer phases, in various stages of polymer curing.[123] They find that a low concentration of Zn, in certain polymer phases, has the effect of reducing the curing rate. These experiments have the potential to determine methods to increase the rate of curing and hence the production rate of some polymers by selecting methods which have high concentrations of Zn in appropriate phases.

Since SIMS is a highly sensitive surface technique, it has also been used to probe the composition of the surface of a variety of samples. In particular, SIMS has been used to compare surface versus bulk properties of a polymer, since the surface of a material has a strong influence over how it interacts with the environment. Imaging TOF-SIMS of a blend of poly(vinyl chloride) (PVC) and PMMA, coupled with shallow depth profiling, demonstrates that the surface of the copolymer is composed of PMMA, whereas the bulk is composed of phase-separated PVC and PMMA.[124] Marien et al. used SIMS to characterize a diblock copolymer by obtaining depth profiling images.[125] These images also showed that the surface of the polymer, which is composed of fluorinated chains, is different from the bulk, which contains micron-sized fluorinated phases in PMMA. Bulk characteristics determine the way a material will function. However, the surface chemistry determines how it will interact with the environment. These issues are especially important for biomaterials applications.[126]

Galuska examined the molecular weight of a polymer on the surface of polypropylene (PP) fibers since the molecular weight influences the properties of nonwoven PP fabrics.[127] He used a novel method of determining the molecular weights based upon relative fragment ion intensities for molecular weights less than 20 000 Da. In this study, the melt-blown fibers have lower molecular weight polymers on their surfaces than the spun-bound polymers. This study exploits the extreme surface sensitivity of TOF-SIMS and results in the correlation of processing conditions and resin type with polymer molecular weights.

Metal−polymer interfaces have also been studied by SIMS. The degree of metal coverage in a metallized polymer determines the final quality of the product, which is significant to industrial manufacturers. A study by Travaly and Bertrand demonstrated that Al reacts with the oxygenated moieties of poly(ethylene terephthalate) (PET) and PMMA, inducing uniform growth of Al on the polymer surface.[128] The interaction of Cu with these polymers is quite different. A weaker interaction of Cu with the polymer causes Cu to cluster on the polymer surface producing a lower quality product, indicated by imaging TOF-SIMS data.

Molecular identification of active members of bead-bound combinatorial libraries is an application well suited to imaging SIMS.[129−131] Covalently bound molecules are first chemically cleaved from resin beads with appropriate linkers and then imaged directly on bead surfaces. Three beads, two coated with phenylalanine (green) and the other with leucine (red), are shown in Figure 12,[129] demonstrating the potential of imaging SIMS to simultaneously characterize multiple beads in one image field. Each bead contained only femtomole quantities of peptide. These experiments indicate that analysis could occur as fast as 10 beads per second.

B. Thin Films

Imaging SIMS is ideally suited to the application of thin films due to its surface sensitivity. Two major types of thin films, which will be reviewed here, are Langmuir−Blodgett (LB) films and self-assembled monolayers (SAMs). The LB films are ordered arrays of amphiphilic molecules physisorbed on surfaces of appropriate polarity. The SAMs are ordered arrays of molecules that are chemically bound to surfaces. Typically, the molecules of interest in both of these cases are long-chain molecules. The SAMs can be patterned, through a variety of techniques, and have

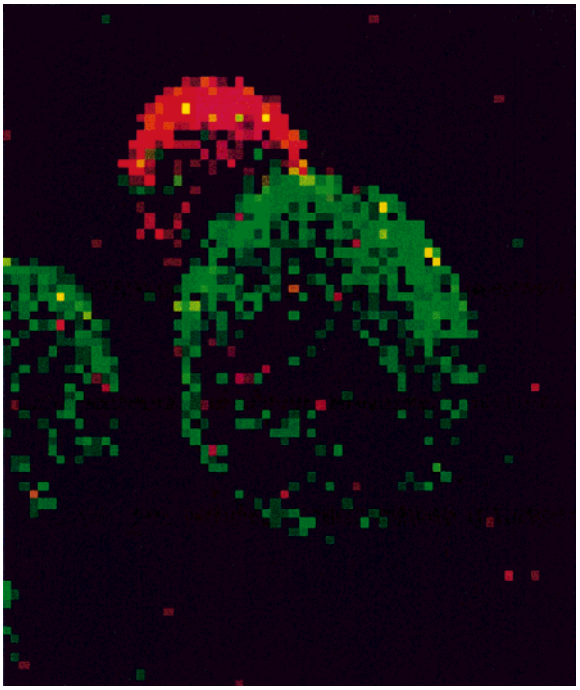

Figure 12. TOF-SIMS image of a mixture of beads with covalently bound amino acids, after vapor-phase clipping. The $(M + H)^+$ ion intensity for phenylalanine is shown in green, while the $(M + H)^+$ ion intensity for leucine is shown in red. The more brightly colored pixels contain more than one count. The primary ion beam is incident 45° from the surface normal (from the top). The field of view is 120 μm. (Reprinted with permission from ref 129. Copyright 1994 American Association for the Advancement of Science.)

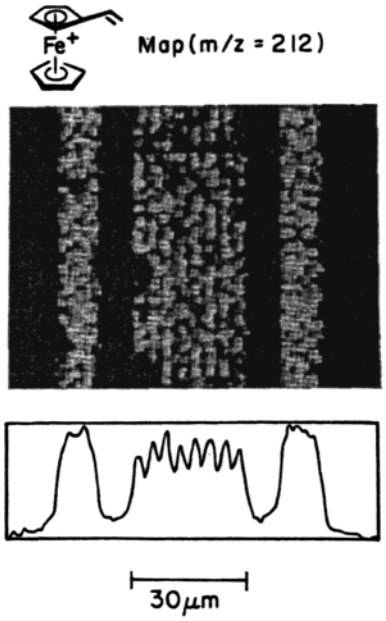

Figure 13. SIMS map of a vinyl ferrocene fragment, *m*/*z* 212, from a Au−I SAM photopatterned with reagent V. The map covers approximately 7×10^{-6} cm^2 and was acquired in 26 s using a 50 pA, 16 keV Ga^+ beam. The total dose to the surface was 1×10^{15} ions/cm^2. The image was subjected to a smooth. The software-produced composite line scan highlights the positions of the 2 μm wide lines in the center of the image.[137]

been characterized using imaging SIMS. Patterned monolayers have potential applications for biosensors and microelectronic devices.

Defects and folds in LB films have been imaged by Hagenhoff and co-workers.[132] They find that layers of stearic acid have defects less than 1 μm in size, whereas films of poly(methyl acrylate) are homogeneous in distribution. Kidney-shaped domains of fluorescently labeled lipid molecules (nitrobenzoxadiazolphosphatidylcholine, NBDPC) and dipalmitoylphosphatidylcholine (DPPC) in LB films have been imaged using TOF-SIMS analysis.[133] The large fluorescent tag on NBDPC is thought to cause steric hindrances and therefore this molecule is only found in the liquid expanded regions of the film, and not the liquid concentrated regions of the film. Other work from this group showed pure DPPC films with round domains.[134]

The SAMs are usually patterned by depositing a film of one chemical composition, damaging that film in some pattern, and then depositing a second chemical, which self-assembles, in these damaged areas. Microlithographically synthesized microwires of Au coated with thiols were chemically imaged by Frisbie and co-workers.[135] They also imaged photopatterned SAMs based on signal from $C_{12}H_{12}Fe$ originating from the chemically bound thiol.[136,137] The 2 μm lines patterned on the SAM can be seen in Figure 13, with a line scan of the ion intensity shown below. Gillen and co-workers have also characterized photopatterned SAMs[138,139] and ion and e-beam patterned SAMs[140] using imaging SIMS. Patterned silanes and metallized Si surfaces were the topic of yet another study.[141] The results of these studies show that two different compounds form well-defined domains and that there is little mixing during the lithographic process.

In a study aimed at applications in molecular electronics, Au and indium−tin oxide (ITO) electrodes were simultaneously exposed to a solution of two different chemicals.[142] The thiols preferentially bind to the Au surfaces and the carboxylic or phosphonic acids bind to the ITO surfaces. The selective bonding of two molecules to two substrates from the same solution is called orthogonal self-assembly. Both of the bonded chemical species and the substrates were characterized using imaging SIMS. This mode of self-assembly allows an individual molecule to connect two electrodes.

A novel application of imaging SIMS utilizing SAMs is the study of electron scattering from an electron beam, from an environmental scanning electron microscope (ESEM), based on the damage the beam creates in the SAM.[139,143,144] The electron beam causes damage in a F-containing SAM beyond the dimensions of its raster pattern. A blooming effect of the electron beam is represented by a reduction in fluorine signal in an area larger than the raster pattern of the electron beam.[144] Electron scattering was further studied by comparing the damage of an electron beam spot on a SAM in a high vacuum environment, where there is low scattering, and at a higher pressure (20 Torr of H_2O), which exhibits increased electron scattering. Imaging SIMS demonstrates that prolonged electron-beam exposure causes the deposition of an O layer on the surface. Lines were also drawn on an alkyl-derived SAM with

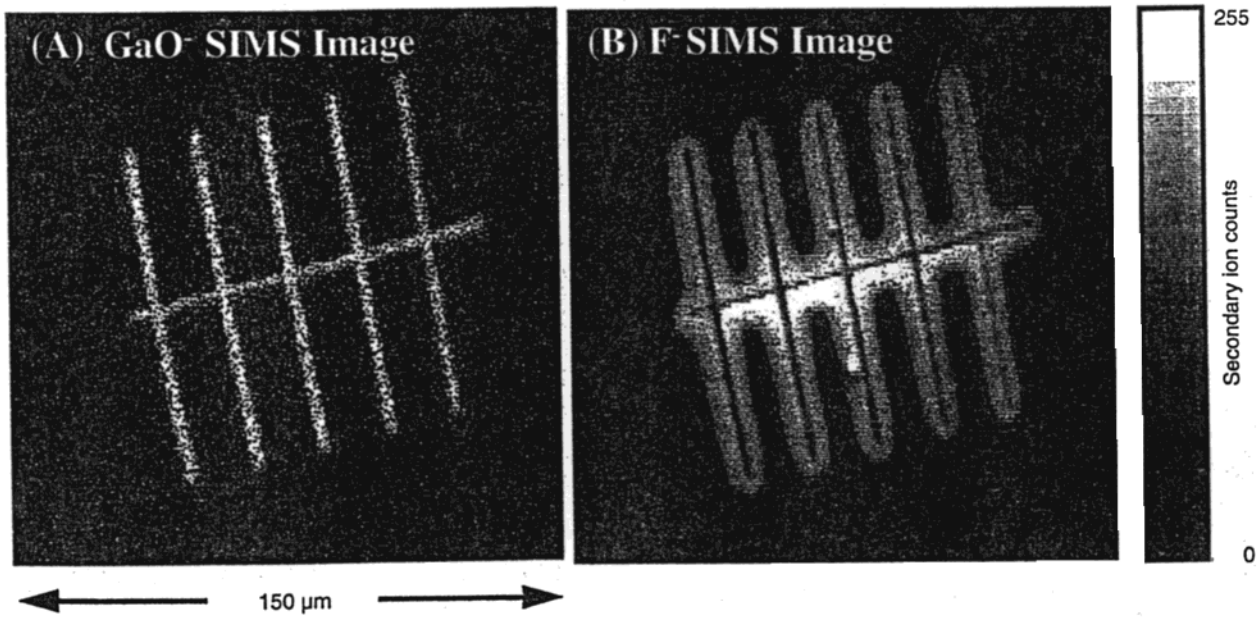

Figure 14. Secondary ion mass spectrometry image of a series of lines drawn in a self-assembled monolayer film with a focused liquid metal gallium ion gun. The GaO^- signal shows the distribution of the bulk of the primary ions. The F^- signal maps the regions of the sample exposed to ion bombardment and is used to visualize the extended tails of the primary ion beam profile. Horizontal field of view 150 μm. (Reprinted with permission from ref 143. Copyright 1998 Foundation for Advances of Medicine and Science.)

a Ga^+ ion beam. This sample was then treated with a thiol-containing F that deposited in the damaged areas. Imaging of the F profile using SIMS depicts the tails of the primary beam profile as shown in Figure 14.[143]

C. Paper

Paper is a plant-based material which is often treated with polymers and other organic materials and therefore, well suited to imaging SIMS characterization. The composition and distribution of surface components determine the print quality and appearance of paper. Two types of paper have been characterized with TOF-SIMS; high-quality print paper, with a mottled print appearance, and spotted uncoated label paper.[145] A comparison of the mottled areas of the print paper to unblemished areas showed Ca spots on the paper and an inhomogeneous distribution of hydrocarbons from the latex coating on the mottled section. Imaging is crucial to determining the cause of the spotting in this case. The authors note that a comparison of the mass spectra from both papers showed some differences in peak intensities, but no extra peaks between the two spectra. Spots on the uncoated label were characterized and found to contain high levels of poly(dimethylsiloxane)s. The authors determined the source of these species to be the release sheet used in processing and not the adhesive side of the label.

Sizing agents are chemicals applied to paper to increase the water resistance of the paper. Therefore, imaging paper surfaces that have been chemically treated and characterized according to their sizing ability allows correlation of surface composition with sizing. Brinen and Kulick determined that areas of treated paper with improved sizing contain fewer high mass species and high mass-containing aggregates on the surface compared to untreated paper.[146] The chemical identification of the high-mass species, which SIMS images linked to sizing, was proposed. Ozaki has also characterized rosin-sizing agents on the surface of paper using TOF-SIMS, EPMA, and XPS.[147]

V. Imaging of Biological Materials

The possibility of directly discerning the spatial distribution of chemical components in cells and tissues is an exciting possibility. With careful sample preparation, images of ion distributions, pharmaceutical distributions, native organic compounds, and externally applied pollutants can be obtained using imaging SIMS. Progress in bioapplications of imaging SIMS is rapid, with many researchers making significant contributions to physiology, toxicity, pharmacology and biochemistry.

A. Plant Cells and Tissues

Chemical imaging of plant roots, shoots, and seeds using SIMS has provided direct evidence for the spatial distribution of both endogenous and exogenous species within these structures. Four plant studies using dynamic SIMS have been recently reviewed.[148] These include metabolic studies using N-labeling, Ca distributions in cell walls, and the distribution of ions in seeds. Fragu and co-workers have also reviewed SIMS imaging of plants, including a discussion of sample preparation and N-labeling experiments.[149]

Sample preparation is now recognized as the key to successful plant chemical distribution experiments. Lazof and co-workers have rated the properties of different root tissue types of freeze-dried cryosections based on several factors of cell preservation, which

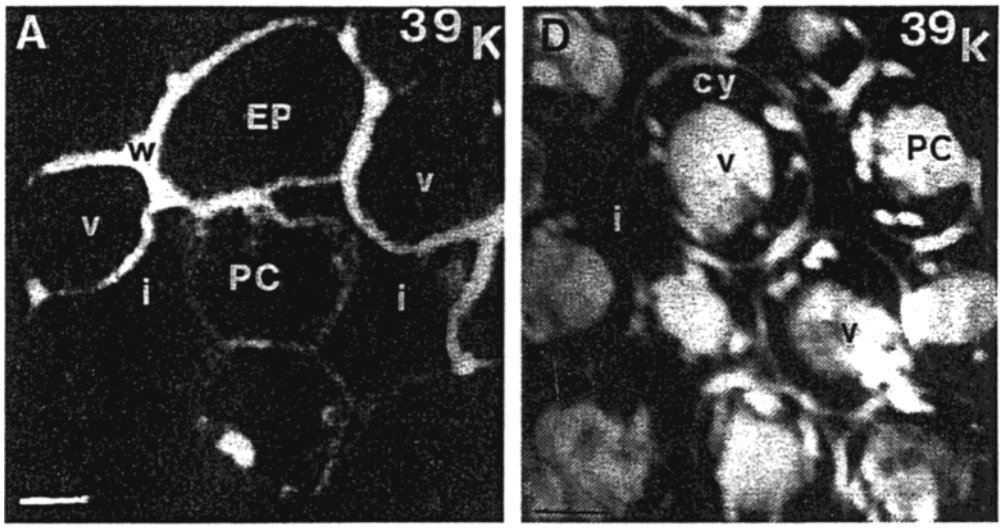

Figure 15. Comparison of chemical fixation (A) and cryofixation (D): SIMS images of ^{39}K localization. Bar: 6 μm. (A) Field of epidermis and parenchyma cells for K, which is localized at the periphery of the cell. (D) Parenchyma cells where K is in the vacuoles, in the cytoplasm as bright spots and near the periphery of the cells. EP: epiderm, PC: parenchyma cell, w: cell wall; cy: cytoplasm, v: vacuole; I: intercellular spaces. (Reprinted with permission from ref 152. Copyright 1997 Royal Microscopical Society.)

can be generalized as goals for all methods of sample preparation for imaging SIMS.[150] These factors are morphological preservation, sample integrity under ion bombardment, minimal sample contamination, minimal redistribution of diffusible species, and practicality for routine analysis. Three different sample preparations have also been compared based on the distribution of Ca in flax seedlings.[151] In general, the authors prefer cryogenic methods to chemical fixation for imaging SIMS analysis because of the superior preservation that cryogenic methods provide. Although many research groups do not currently have the capability to examine frozen samples, this option is becoming commercially available on SIMS instrumentation. Dehydrating plant samples to make them vacuum compatible will no longer be necessary, and the standard approach will probably shift toward frozen-hydrated sample analysis.

Fragu and co-workers compared two methods of sample preparation for soybean leaves: chemical fixation followed by chemical substitution and cryofixation followed by chemical substitution.[152] A comparison of the K distribution for the two methods of preparation is shown in Figure 15. In the case of chemical fixation, Figure 15a, the K is found in the cell periphery, the cytoplasm and the cell wall, but not in the vacuole. In contrast, the sample prepared by cryofixation shows a distribution of K in the periphery of the cell, dense spots in the cytoplasm and within the vacuole, which is in agreement with the known physiological distribution of K. Other elements including Ca, Mg, P, S, ^{15}N, and ^{14}N have also been examined. In addition, the authors propose that the ratio of K to Ca in the cell may indicate the preservation of cell integrity.

The spatial distribution of K, Na, Mg, and Ca ions in birch pollen has been examined by SIMS using pollen prepared by nonaqueous chemical fixation methods to reduce the potential for ion redistribution.[153] The data, with K and Na localized in some structures and Mg and Ca localized in different structures, exhibits the same distribution as obtained using cryofixation and bulk analysis methods. This study shows the potential of SIMS imaging in applications of germination and pollen tube growth through the study of ionic distributions.

The study of endogenous chemicals has been the topic of several plant-based studies. Mechanical pulp from jack pine sapwood is treated with hydrogen peroxide to brighten the material. Because metals catalyze a decomposition reaction of pulp with peroxide, SIMS was used to map the distribution of Ca and Mn, which were found in the torus, ray parenchyma cell wall, cell corners, and middle lamella.[154] An earlier study by the same researchers determined that Ca, Mn, and Fe are localized in the torus, middle lamella, cell corner, and ray cell wall of the black spruce.[155]

Calcium is one of the major plant nutrients and has been the focus of several plant-based SIMS studies. Calcium plays an important structural role in the cross-bridging of cell wall pectins and also has a role as an intracellular messenger. For these reasons, Gea et al. compared the endogenous Ca distribution in roots of pine with and without fungal growth.[156] The results suggest that the Ca moves from the root to the fungus, causing cell separation and allowing fungal penetration. An early study of root cap cells by Chandra and co-workers localized Ca in the slime around the root cap, and in the cell walls, nuclei, and amyoplasts.[2] In another study, ^{44}-Ca was applied to mature apple fruits to study the mechanisms of Ca uptake.[157] Imaging SIMS indicates that ^{44}Ca is localized to small microdomains in the cell walls, leading them to the conclusion that Ca has an important role in ripening of fruit. An earlier study examined the distribution of Ca in ripe cherry tomato fruits.[158]

Lazof and co-workers have studied Al toxicity in soybean root tips using freeze-dried cryosections.[159−161] These studies offer the first direct evidence that Al

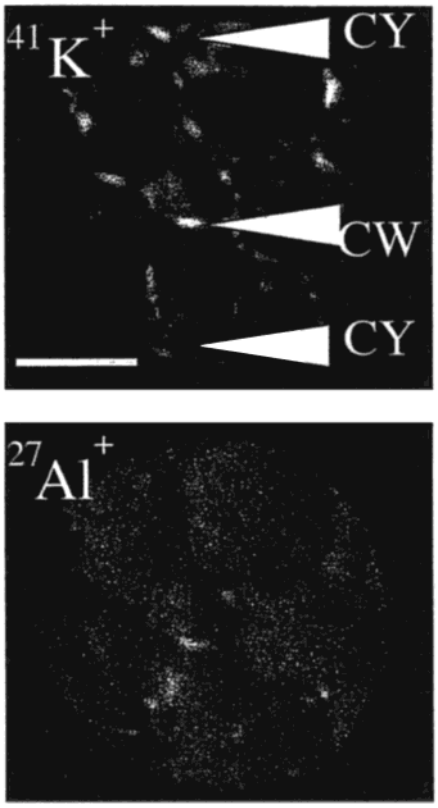

Figure 16. A SIMS image set collected in the mid-cortical region of a freeze-dried cryosection from the mature region of a soybean root. Included are secondary ions from K and Al. Areas of cell wall (CW) and probable cytoplasmic deposit (CY) have been designated. The images have been enhanced (each with the identical adjustments) for clarity of photoreproduction. Bar = 50 μm. (Reprinted with permission from ref 160. Copyright 1997 Springer Verlag.)

penetrates the cell interior and is not solely confined to the extracellular space, as shown in Figure 16. An understanding of the distribution of Al in root tip cells provides information about the mechanism of early Al toxicity in plants.

B. Animal Cells and Tissues

Chemical imaging using mass spectrometry of animal cells and tissues is an emerging field. Most experiments to date using dynamic SIMS have been confined to elemental analysis. Many other analytical imaging strategies rely on chemical labeling. Radiolabeling typically requires a long time scale for analysis and is expensive. Fluorescence experiments can be performed on living cells, but rely on an inherently fluorescent molecule of interest or a fluorescently labeled molecule, which may not have the same action as its unlabeled analogue. In addition, fluorescence may be quenched by the chemical environment. On the other hand, SIMS analysis can be performed on a short time scale, is very sensitive, and can detect all elements and isotopes.

Sample preparation is of paramount importance to the validity of biological imaging SIMS experiments. The topic of sample preparation has been the subject of many studies.[162−169] In particular, one report by the IUPAC Commission on Microchemical Techniques & Trace Analysis reviews the sample requirements, recommends methods of sample preparation, and discusses potential artifacts common to these experiments.[169] Samples must be conductive, vacuum compatible, and relatively flat, without affecting the chemistry and structure of the cells or tissues. Varieties of methods have been used to prepare samples to meet these requirements. The most common protocol used today is that of fast freezing and freeze-drying, although some experiments have recently been conducted on freeze-fractured, frozen-hydrated samples.[170−173] The report also illustrates artifacts arising both from sample preparation, such as ion redistribution and structural damage, as well as from the analysis method, such as matrix effects, mass interferences, preferential sputtering, and differing ion yields.

Fast freezing is critical to sample preparation because it rapidly stops all cellular chemical processes and minimizes artifacts. Freezing on time scales that are too slow results in the formation of ice crystals that can distort cell shapes.[165] Semicryogenic methods such as freeze substitution and freeze-drying after plastic impregnation often result in the redistribution of ions. Chemical fixation causes ion redistribution and results in physiologically meaningless ion images.

It is important to determine that the cells have not been damaged due to the preparation process to acquire physiologically valid chemical distributions. In Figure 17, the Na and Ca distributions in fractured C11 hepatocytes are shown.[163] The cell on the left is an injured cell and the one on the right is healthy. Healthy cells typically have a low Na/high K ratio. However, the damaged cell on the left has a high amount of Na. In addition, there are Ca spots in the damaged cell which correspond to the accumulation of Ca in mitochondria after cell injury.

1. Pharmaceuticals

An area in which SIMS has made a particularly significant contribution is the cellular and subcellular monitoring of pharmaceuticals. Typically, these studies rely upon the drug containing an atom that is not natively found in cells or tissues. By studying the distribution of one atom, the distribution of the drug, and in some cases its metabolites, can be determined. Morrison and co-workers have characterized the distribution of *p*-boronophenylalanine−fructose (BPA-F), a boron-containing drug in clinical trials, in brain and brain tumors (glioblastoma multiforme).[174−176] The drug BPA-F is used in boron neutron capture therapy, by delivering boron to neoplastic cells. Boron captures a neutron and emits a heavy, high energy, charged particle, which causes cell death. Their studies show that BPA-F is strongly localized in the tumor tissue.[174] Most importantly, B is also found in small neoplastic clusters, away from the main tumor, which cannot be removed surgically. These clusters are invasive and are the reason for the reoccurrence of glioblastoma multiforme. This finding demonstrated the great impact BPA-F could have in brain cancer treatment and the utility of imaging SIMS in determining the distribution of pharmaceuticals.

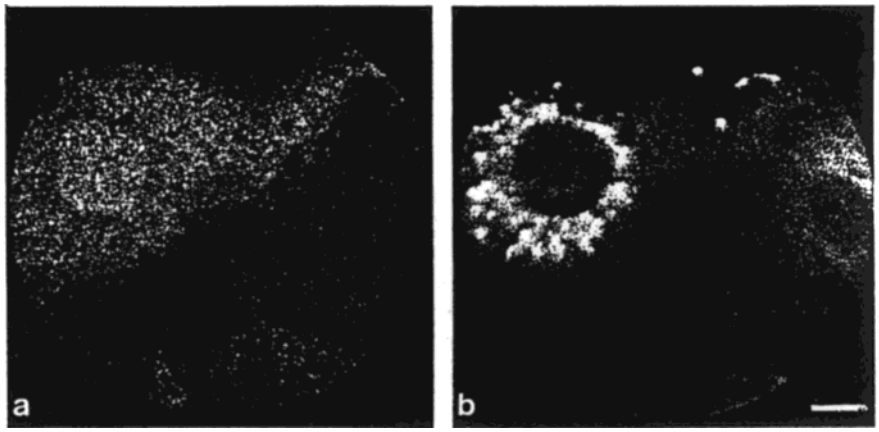

Figure 17. $^{23}Na^+$ (a) and $^{40}Ca^+$ (b) ion micrographs of adjacent injured (left) and healthy (right) fractured C11 hepatocytes showing the mitochondrial accumulation of calcium that can result from cell injury. Photographic exposure times = 0.5 and 100 s, respectively. Bar = 10 μm. (Reprinted with permission from ref 163. Copyright 1989 Royal Microscopical Society.)

Another study demonstrates the feasibility of employing imaging SIMS to identify the distribution of halogen-containing drugs in tissue. Human red blood cells infected with the malaria parasite are treated with mefloquine, a fluorine-containing compound.[177] For these cells, the fluorine signal appears homogeneously in uninfected red blood cells and is localized in the food vacuole, cytoplasm and nucleus of the parasite in infected cells. Signal from CN can be seen localized to the parasite, as well as P in the parasite nucleus and F from mefloquine, in Figure 18. The nucleus of the parasite is confirmed to overlap with the fluorine signal by labeling it with the compound IdU (5-iodo-2′-deoxyuridine), a DNA tag, and monitoring I signal. The localization of mefloquine in the parasite will help researchers understand the mode of action of the drug.

Fragu and co-workers studied the distribution of iodine from the drug metaiodobenzylguanidine (MIBG) in human neuroblastoma cells, which were xenografted into nude mice.[178] The drug MIBG kills tumor cells because ^{131}I is incorporated in the molecules and emits particles. This study demonstrates the importance of cryopreparation of samples. Rapidly frozen, cryoembedded cells exhibit I in the cytosol and perinuclear region, depicting normal physiology, whereas chemical fixation causes a redistribution of I in the nuclei. There is a nonuniform distribution of MIBG in the tumor, explaining the inefficiency of the drug in cancer treatment since it does not penetrate all parts of the tumor. The authors conclude that a drug with a radionucleotide that emits at a range longer than ^{131}I would be more effective for cancer treatment.

Imaging SIMS is often used to complement other techniques, such as fluorescence imaging. Two cancer drugs, pazelliptine and intoplicine, both exhibit native fluorescence. Guerquin-Kern et al. studied human mammary tumors with SIMS and fluorescence imaging.[115] However, DNA quenches the fluorescence of both drugs, limiting the use of fluorescence to determine the presence of the drugs in structures such as nuclei. ^{14}C-labeled intoplicine is not seen in the nucleus using fluorescence, but is shown to be present in these organelles using imaging SIMS. The SIMS data from pazelliptine is not conclusive, because no signal is found in the nuclei as is expected, but the authors believe that they might not have eroded the nuclei to the proper depth. This study demonstrated the advantages of using both SIMS and fluorescence to determine the distribution of an anticancer drug.

Another pair of pharmaceuticals, used as anxiolytic, anticonvulsive, and hypnotic agents, has also been investigated using imaging SIMS.[179] The distribution of the F-containing flunitrazepam (benzadiazepine) and triflupromazine (phenothiazine) was determined directly, in three central nervous cell systems, C6 glioma cells, primary astroglial cells, and neuroblastoma (B104) cells. The images show that flunitrazepam is concentrated in the nucleus, and in some cases in the nucleoli, for all three cell lines. Images from cells treated with triflupromazine show the distribution of F to be solely in the cytoplasm of the cells, suggesting a different mode of action than that of flunitrazepam.

2. Ion Transport

Imaging SIMS has been used to study ion transport in organisms, typically by isotopic labeling. Of particular interest is the development of a method to monitor Mg, an important nutrient. There are no long-lived isotopes of Mg available, which impedes the progress of research. Morrison and co-workers have studied the transport of the stable isotope ^{26}Mg in the kidneys of killifish using imaging SIMS.[180,181] They find Mg in the proximal tubule and collecting duct of the kidney. Proximal tubules had been known to secrete Mg, but the presence of Mg in the collecting duct had been unknown. The authors propose that the collecting duct may be a site of Mg resorption and work along with the proximal tubule to regulate Mg.

3. Pollutants

Freshwater pollutants can be studied by investigating their distributions in vertebrate and invertebrate tissues or organisms exposed to the pollutants. A number of examples of metal accumulation have been characterized using imaging SIMS and

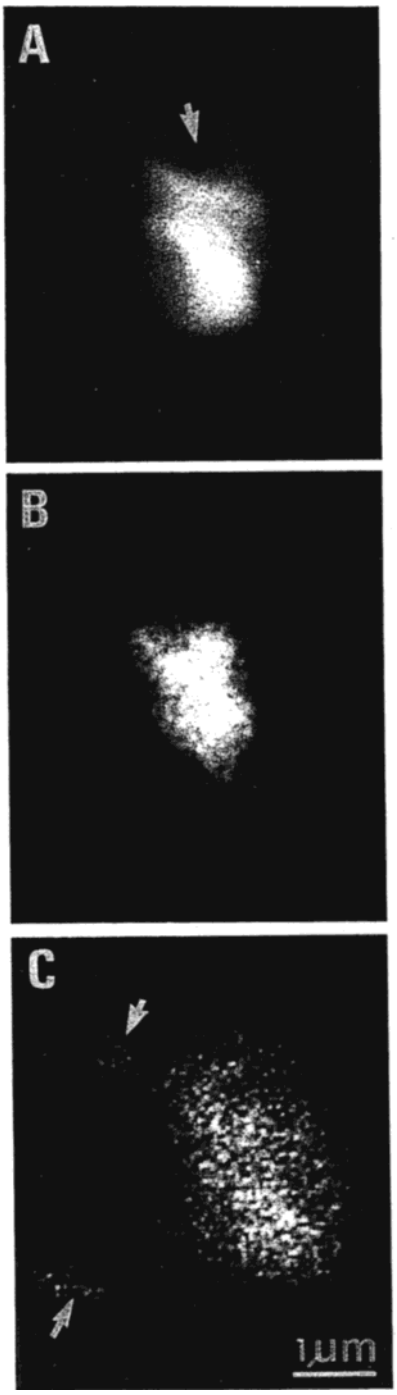

Figure 18. Image of a *P falciparum* infected red blood cell incubated with mefloquine. (A) Computerized images of $^{26}Cn^-$ showing the parasite and its food vacuole (arrow). (B) Computerized images of $^{31}P^-$. (C) Computerized image of $^{19}F^-$ showing the presence of the drug in the parasite and in the cytosol of the infected erythrocyte (arrows). (Reprinted with permission from ref 177. Copyright 1994 Elsevier.)

EPMA.[182] Bivalves exposed to metal pollution were found to have elevated concentrations of Al, Cu, Fe, and Li in their digestive glands. Lysosomes of epithelial cells from labial pulp in bivalves contain Cr after exposure to Cr-doped water.[182] In addition, aluminum toxicity is currently a subject of great interest to physiologists. Trout are found to have Al concentrated in both gill and kidney lysosomes, a type of excretory organelle.[182] In contrast, homogeneous distributions of Al are seen in bone, heart, and brain tissue of trout.

4. Hard Tissues

The distribution of ions in bone and tooth[183−185] has been the topic of many recent imaging SIMS articles. Levi-Setti and co-workers have had a particular interest in the surface ion composition of bone in various stages of acidosis (conditions of lower than physiological pH).[186−191] The bone surface ion composition can lead to an understanding of the mechanism of bone loss. Metabolic acidosis led to a release of bone Ca and Na in mouse calvariae.[186] However, the ratio of Na/Ca decreases relative to the ratio found in normal bone. These data suggest there is a greater release of Na than Ca. When bone-resorbing cells (osteoclasts) are treated with the chemical calcitonin, the Na/Ca ratio in metabolic acidosis does not change as compared to the ratio in normal cells. Calcitonin is known to inhibit osteoclasts, so the greater amount of sodium released in the first case seems to be a result of the functioning osteoclasts. Respiratory acidosis, on the other hand, is shown to cause less Ca loss and little change in the Na/Ca ratio compared to the control situation.[191] The effect of Al on bone has also been considered.[189] Results of these experiments show that Al causes Ca loss from bone, along with greater loss of Na and K, which is consistent with theory.

5. Thyroid

The study of thyroid and goiter organified I distributions, 99% of all thyroid I, had recently been reviewed by Fragu and co-workers.[192−195] Three types of follicles from goiterous thyroid glands were compared using imaging SIMS.[193] Different follicle types are known to have varying iodine turnover rates and structures, which is confirmed in this study. By labeling the follicles with ^{125}I in vitro, a comparison of pretreatment iodine distributions (^{127}I) and post-treatment iodine (^{125}I) distributions could be made. Some follicles from the goiterous tissue are found to function normally, although the ^{127}I concentration is lower than in normal tissue. Other follicles were interpreted to have an inability to trap iodine because they have a complete absence of both ^{127}I and ^{125}I. Characterization of the function of follicles leads to a greater understanding of diseases of the thyroid.

6. Chromosomes

Identifying defects in genes is critical to our understanding of genetic diseases. Levi-Setti and co-workers have studied chromosomes using imaging SIMS by labeling DNA with bromodeoxyuridine (BrdU) and monitoring Br signal.[196−199] In addition, ^{14}C labels were used to identify the DNA, RNA, and protein content of the chromosomes. The authors find banding in Mg and Ca SIMS images that correlated with similar banding patterns seen in optical staining methods. These data indicate the cause of the banding in optical staining could indeed be from the replacement of divalent cations by the Geisma stain. Of particular interest to these investigators is the identification of fragile sites and sister chromatid

Figure 19. High-magnification image. Color-coded superposition showing $^{81}Br^-$ (green) and $^{26}Cn^-$ (blue) SIMS maps of portion of a BrdU-labeled mitotic cell cultured in the presence of the chemical aphidicolin, an inhibitor of DNA replication. Five examples of SCE and one centromeric twist can be identified in this image. The field of view is 17 μm wide. (Reprinted with permission from ref 197. Copyright 1996 CMB Association.)

exchange (SCE) in chromosomes.[197] The distribution of the label (^{81}Br) in green and the chromosome (^{26}-CN) in blue is shown in Figure 19.[197] A centromere twist can be seen in the large, middle chromosome on the right. Sister chromatid exchange is evident in the chromosome just to the left of the centromere-twisted chromosome as well as on several other chromosomes. Since these defects are chemically induced, the study suggests the application of SIMS screening for mutagenic properties of chemicals. Similar experiments have also been published by another group.[200]

7. Molecular Imaging

Only recently has imaging SIMS been applied to acquire molecular images of biological materials.[201] Developments in this area hold the promise of direct identification of molecular components. Todd and coworkers have investigated the distribution of phosphocholine in the dog adrenal gland and mouse brain.[201,202] Since these static SIMS experiments are highly surface sensitive, sample preparation is of crucial importance.[170,171,173] Samples must be prepared in a manner that introduces no contamination. Fast-frozen, freeze-fractured biological samples are characterized by scanning electron microscopy because of the minimal effect on the sample.

Freeze-fractured, frozen-hydrated analysis of membranes, similar to SEM preparations, has been the focus of several experiments by Winograd and coworkers.[170−173] Preliminary experiments of freeze-fractured, frozen-hydrated paramecia show images

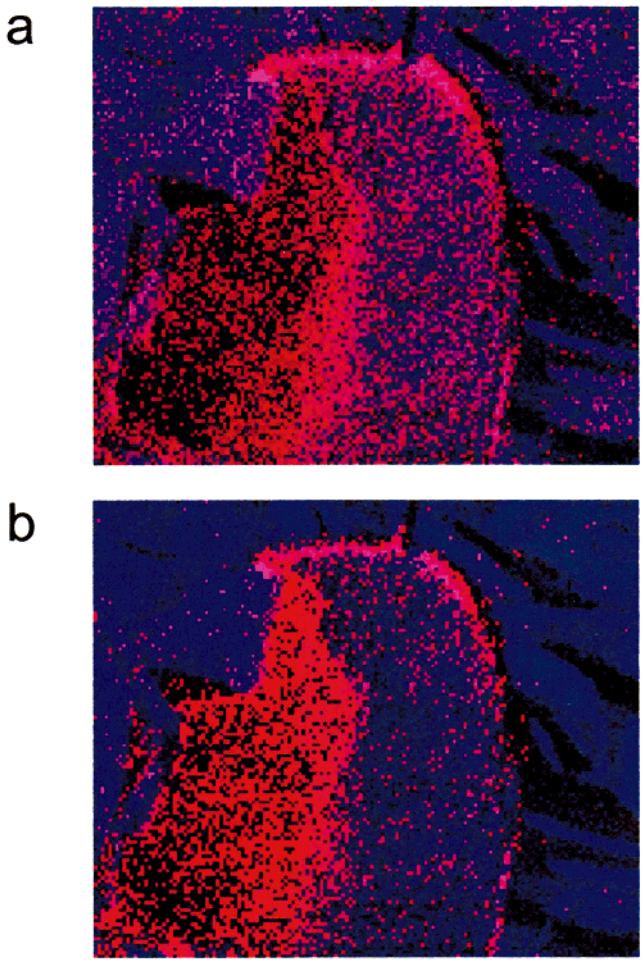

Figure 20. TOF-SIMS images of a freeze-fractured, frozen-hydrated paramecium. Blue represents water, and red represents C_2 hydrocarbons in (a) and K in (b). Field of view is 67 μm.[171]

of C_2 hydrocarbons and K in Figure 20, a and b, respectively.[171] These early studies also probed the distributions of dopants, dimethyl sulfoxide and cocaine, in paramecia. Later experiments demonstrated the ability to obtain molecule-specific images of lipids from freeze-fractured, frozen-hydrated liposomes (synthetic lipid membrane spheres) and red blood cells.[170,172,173] Images of a dipalmitoylphosphatidylcholine (DPPC) liposome are shown in Figure 21.[170] The images show a distribution of phosphocholine headgroup-related fragments across the surface of the liposome. Water is shown in blue, indicating that the fracture event did not result in dehydration of the surface or deposition of water on the surface, covering all features of interest. Their experiments resulted in the first images of molecular signal from freeze-fractured, frozen-hydrated analysis of biological samples.

VI. Imaging Using Lasers

The use of lasers in imaging MS can have several advantages over the use of ion beams alone. These include very high sensitivity, selective ionization, quantification, high mass resolution, and little influence from matrix effects. Desorption of neutrals can be accomplished using an ion beam or a laser beam. Ionization of neutral species in order to use mass spectrometry as the method of detection involves electron beams[34,203] or lasers.[24,60,204−206] Yet another MS method, MALDI, has shown promise for imaging.

Savina and co-workers have investigated the use of laser desorption coupled with laser ionization using two separate lasers.[205,207] A fractured rubber−brass interface was examined. Sulfur oxide was confined to the brass areas and the authors proposed that SO may contribute to joint adhesive failure. Berthold and Wucher used ion beam desorption/laser ionization to image metal grids.[206] Their goal was to optimize the technique for acquisition time and sensitivity. Winograd and co-workers have also been investigating femtosecond lasers to ionize sputtered neutral molecules with minimal fragmentation.[24,61,131,208] Their experiments show high sensitivity and spatial resolution.

An example of the reduced influence of the matrix upon sputtered neutrals can be seen in Figure 22 by comparing SIMS and SNMS data.[60] Polystyrene (PS) was applied to a Si substrate in a manner that produced small dots (<10 μm) surrounded by a thin homogeneous covering of PS. The images from laser ionization of the sputtered neutrals in the top row clearly show a higher intensity of PS-derived fragment ions from the dots than from the background. In this case, the postionized neutral intensities reflect the surface concentration. However, the SIMS images imply the reverse, and misleading, circumstance as shown in the lower set of images. The thin PS layer over the Si substrate yields higher PS-derived signal than from the thick PS dots. This experiment clearly

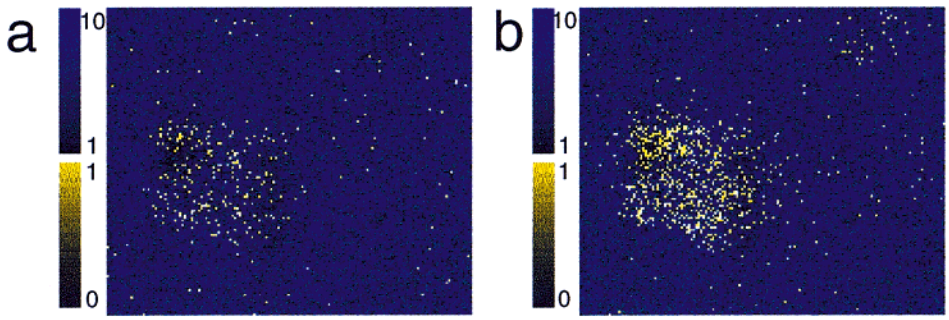

Figure 21. Freeze-fractured frozen-hydrated dipalmitoylphosphatidylcholine liposome. Field of view is 143 × 117 μm. (a) Water in blue (*m*/*z* 18, 19), phosphocholine fragment in yellow (*m*/*z* 166), (b) water in blue (*m*/*z* 18, 19), phosphocholine headgroup in yellow (*m*/*z* 184). Note that the intensity of water is decreased over the liposome where the intensities of *m*/*z* 166 and 184 are greatest. +SIMS mode. (Reprinted with permission from ref 170. Copyright 1998 John Wiley and Sons.)

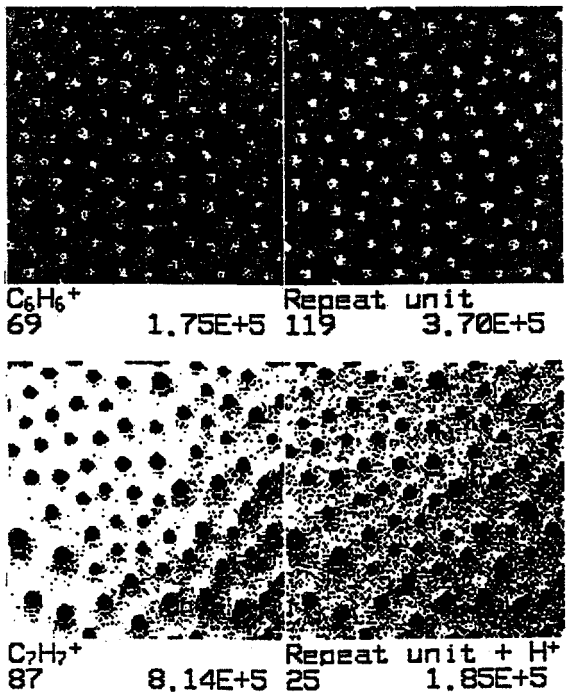

Figure 22. Laser SNMS (above) and SIMS (below) molecular mapping of polystyrene dots on an Si wafer. Field of view is 130 × 130 μm^2, 128 × 127 pixels. Laser SNMS: one cycle per pixel (1 μs pulse width), image acquisition time 28 min, primary ion dose density 3×10^{11} cm^{-2}, sample consumption <1% of the outer monolayer, SIMS: 500 cycles per pixel (200 ns pulse width), image acquisition time 30 min. primary ion dose density 3×10^{13} cm^{-2}, sample consumption ~30% of the outer monolayer. (Reprinted with permission from ref 60. Copyright 1992 John Wiley and Sons.)

demonstrates the minimal influence of the matrix on the emission of sputtered neutrals.

Arlinghaus and co-workers compared sputter-initiated resonance ionization microprobe (SIRIMP) and laser atomization resonance ionization microprobe (LARIMP) techniques to characterize the distribution of undecahydromercapto-*closo*-dodecaborate (BSSB), a boron-containing drug used in boron neutron capture theory, in rat tissues.[209] From their work, they propose that LARIMP is a much faster method of analysis, but only offers cell-sized spatial resolution. In comparison, SIRIMP has a slower data acquisition rate, yet high spatial resolution and depth profiling capabilities. LARIMP imaging of a rat kidney after BSSB treatment results in a high B concentration in the medulla tube region. The results are physiologically plausible because the kidney is known to remove toxins, such as B, from the blood. SIRIMP imaging of a brain tumor treated with BSSB showed a distribution of high and low areas of B concentration. This experiment demonstrates the potential of LARIMP and SIRIMP imaging for determining the distribution and concentration of B in tissue.

The idea of imaging using MALDI concepts has recently become a subject of interest.[14,210−212] The general protocol involves the application of a thin coat of MALDI matrix to the sample. The chemistry of the sample can then be imaged by rastering a laser beam across the surface, or moving the sample and holding the laser in one place, and acquiring mass spectra from each point. In addition, quantitation can be achieved by comparison to samples of known concentration.

Hercules and co-workers have used this idea to study thin-layer chromatography (TLC) samples.[210,212] Not only does MALDI consume very little of the sample, allowing subsequent analysis, but it also can distinguish between two compounds located in one chromatographic spot, based upon their molecular weight. Samples are prepared by pressing a thin layer of MALDI matrix onto the TLC plate in the presence of extracting solvent. The authors reported little spatial spread of the analytes using this method of sample preparation and imaged spots of bradykinin, rhodamine B, cocaine, and cocaine-d_3 down to femtomolar quantities.[212] Images of the chromatograph spots show intensity variations that could be due to the signal variation associated with the MALDI process or from the actual analyte distribution.

Caprioli and co-workers have applied MALDI imaging techniques to characterize native cell peptides.[14] Human buccal mucosa (cheek) cells were dried, sprayed with MALDI matrix and then imaged. A strong peak at *m/z* 7605 was found to be localized to the cells. Enzyme digestion of saliva was performed since it also contained signal at *m/z* 7605. Analysis of the digestion determined the C-terminal sequence of the protein. Assuming that the peak at *m/z* 7605 had the formula M+H, the C-terminal sequence was used to determine the identity of the peak from a protein database. The most probable match was to a protein involved in the prevention of tooth decay. A recent paper discussed improvements, from hours to seconds, in the rate of image acquisition.[211] Although these types of experiments yield better quality mass spectra and can detect a higher mass range, lateral resolution needs to be greatly improved to be competitive with ion beam approaches.

VII. Conclusions

It is clear from the broad array of examples given in this review that imaging mass spectrometry is having an impact upon a variety of research fields and topics. The drive to characterize chemically heterogeneous features on the nanometer scale makes the availability of this technique even more important. We believe that the implementation of imaging mass spectrometry experiments, however, is at a very early stage. Many of the examples given here are quite application-oriented and do not probe the limits of lateral resolution that is possible. Most of the examples involve detection of elemental species by dynamic SIMS rather than molecular species by static SIMS, and this trend will surely change in the future. In addition, the high surface sensitivity of SIMS is a double-edged sword. The depth from which ions are extracted is very small so the location from which data are obtained is well defined. However, surface contamination of real-world samples, and even those prepared under laboratory conditions, is a very real challenge for analysis. In many cases,

contamination can be minimized by careful sample preparation. There are several areas of research that need careful attention by the SIMS community to accelerate these trends. Some of these are mentioned briefly below.

Sample Preparation. Careful, consistent sample preparation is vital to the success of any surface-sensitive measurement. Static SIMS measurements are particularly affected by sample preparation, due to the sensitivity of the technique to overlayer contaminants. Frequently results from one laboratory are not consistent with another laboratory, even on identical instrumentation, because of differences in sample preparation. For biological samples, proper preparation is especially critical since care must be taken to use methods that minimize changes to the native state of the cells. Sample preparation requires the strictest care when studying diffusible ions and unbound chemical species. Development of cryogenic sample manipulation and cold sample analysis stages and their greater availability suggest that chemical imaging will more often be performed on fast-frozen, freeze-fractured and frozen-hydrated cells.

Quantitative Analysis. Analyte quantification is difficult to accomplish using SIMS analysis, particularly in the static mode. The matrix surrounding the analyte plays a large role in determining the magnitude of ion intensities. Concentrations are usually obtained by comparing the intensity of an analyte to a species of known concentration. The reference species is chosen to have approximately the same chemical characteristics (e.g., ionization potentials and chemical reactivities) as the analyte. Good analytical standards are often not available. In spite of these issues, many workers are uncovering creative strategies for circumventing these problems. Laser and electron-beam ionization of neutrals induced by sputtering offers one potential solution, since the influence of the matrix upon the yield of ejected neutral particles is reduced. Other groups are applying the infinite velocity method to reduce matrix effects and determine concentrations in dynamic SIMS.[213,214]

Molecular Ion Yield Enhancements. Static SIMS measurements do not always yield high molecular and fragment signals for each analyte. Yields are influenced by several factors including sample preparation, the ionization potential of the molecule, and the particular primary ion beam used. Many research groups have focused on improving the signal from static SIMS measurements. Strategies include the use of cluster ion beams and matrix-enhanced SIMS, a technique similar to MALDI.[215,216] Others have exploited the use of laser postionization techniques. More are needed.

Theoretical Advances. An active area of research is the study of fundamental ion−solid and neutral−laser interactions. These experiments coupled with computer simulations provide a better understanding of molecular fragmentation, ejection, and ionization, which should result in better predictions of molecular fragmentation mechanisms.[217] A limiting factor is the availability of accurate interaction potentials which predict the forces between atoms and molecules. Although reliable potentials exist for metals and small organic molecules, there is a special need to model thick organic films, a regime where many studies take place.

Lateral Resolution. Lateral resolution for SIMS analysis has been reported to be as low as 20 nm. Techniques such as SEM, transmission electron microscopy (TEM), near-field scanning optical microscopy (NSOM), and scanning tunneling microscopy (STM) have far better resolution, yet cannot yield the specificity of chemical information that SIMS provides. The advantage of dynamic SIMS compared to other imaging and chemical imaging techniques is that it can directly detect all elements, including those of low mass. Static SIMS measurements produce direct molecular information from surfaces. In part, spatial resolution for ion probe techniques is based upon the primary ion beam spot size. Improvements are still being made in spot sizes of ion sources other than Ga.

Experimental Visions. Applications of imaging MS are diverse. Although we have not offered many examples where the technique has contributed to the solution of fundamental scientific questions, there are many potential (and unexplored) fields in which SIMS is envisioned to make a significant contribution. The strengths of imaging SIMS lie in the ability to spatially determine the chemical distribution with high surface sensitivity. Experiments characterizing diffusion, phase segregation of related molecules, and chemical reaction dynamics are areas which seem rich for exploration.

Many experimental difficulties have been outlined in this review. The ability to acquire images by mass spectrometry from submicron areas provides a novel tool to meet the challenges facing the modern materials chemist. We hope that the perspective gained from examples given here can stimulate new research directions for this powerful strategy.

VIII. Acknowledgments

The authors thank the National Institutes of Health, the National Science Foundation, the Office of Naval Research, and the Clare Boothe Luce Foundation for their financial support. Thanks also go to Michael J. Holland and Alger Pike for their editorial assistance.

IX. References

(1) Castaing, R.; Slodzian, G. *J. Microsc.* **1962**, *1*, 395−410.
(2) Chandra, S.; Chabot, J. F.; Morrison, G. H.; Leopold, A. C. *Science* **1982**, *216*, 1221−1223.
(3) Järås, S. *Appl. Catal.* **1982**, *2*, 207−218.
(4) Liebl, H. *J. Appl. Phys.* **1967**, *38*, 5277−5283.
(5) Levi-Setti, R.; Wang, Y. L.; Crow, G. *J. Phys.* **1984**, *C9*, 197−205.
(6) Benninghoven, A. *Surf. Sci.* **1973**, *35*, 427−437.
(7) Chait, B. T.; Standing, K. G. *Int. J. Mass Spectrom. Ion Phys.* **1981**, *40*, 185−193.
(8) Schwieters, J.; Cramer, H.-G.; Heller, T.; Jürgens, U.; Niehuis, E.; Zehnpfenning, J.; Benninghoven, A. *J. Vac. Sci. Technol. A* **1991**, *9*, 2864−2871.
(9) Benguerba, M.; Brunell, A.; Della-Negra, S.; Depauw, J.; Joret, H.; Le Beyec, Y.; Blain, M. G.; Schweikert, E. A.; Ben Assayag, G.; Sudraud, P. *Nucl. Inst. Methods Phys. Res.* **1991**, *B62*, 8−22.
(10) Andersen, H. H.; Brunell, A.; Della-Negra, S.; Depauw, J.; Jacquet, D.; Le Beyec, Y.; Chaumont, J.; Bernas, H. *Phys. Rev. Lett.* **1998**, *80*, 5433−5436.

(11) Gnaser, H. *Surf. Int. Anal.* **1996**, *24*, 483−489.
(12) Winograd, N.; Baxter, J. P.; Kimock, F. M. *Chem. Phys. Lett.* **1982**, *88*, 581−584.
(13) Pappas, D. L.; Hrubowchak, D. M.; Ervin, M. H.; Winograd, N. *Science* **1989**, *243*, 64−66.
(14) Caprioli, R. M.; Farmer, T. B.; Gile, J. *Anal. Chem.* **1997**, *69*, 4751−4760.
(15) Benninghoven, A.; Rüdenauer, F. G.; Werner, H. W. *Secondary Ion Mass Spectrometry Basic Concepts, Instrumental Aspects, Applications and Trends*; John Wiley & Sons: New York, 1987.
(16) *Secondary Ion Mass Spectrometry*; Vickerman, J. C., Brown, A., Reed, N. M., Eds.; Clarendon Press: Oxford, UK, 1989; Vol. 17.
(17) Benninghoven, A.; Hagenhoff, B.; Niehuis, E. *Anal. Chem.* **1993**, *65*, 630A-640A.
(18) Benninghoven, A. *Angew. Chem., Int. Ed. Engl.* **1994**, *33*, 1023−1043.
(19) Grasserbauer, M.; Friedbacher, G.; Hutter, H.; Stingeder, G. *Fres. J. Anal. Chem.* **1993**, *346*, 594−603.
(20) Bertrand, P.; Weng, L.-T. *Mikrochim. Acta* **1996**, *13*, 167−182.
(21) Benninghoven, A. *Surf. Sci.* **1994**, *299/300*, 246−260.
(22) SIMS, A. e. v. i. d. t. *Int. J. Mass Spectrom. Ion Processes* **1995**, *143*.
(23) Odom, R. W. *Appl. Spectros. Rev.* **1994**, *29*, 67−116.
(24) Winograd, N. *Anal. Chem.* **1993**, *65*, 622A−629A.
(25) Rüdenauer, F. G. *Anal. Chim. Acta* **1994**, *297*, 197−230.
(26) Schueler, B. W. *Microsc. Microanal. Microstruct.* **1992**, *3*, 119−139.
(27) Chabala, J. M.; Soni, K. K.; Li, J.; Gavrilov, K. L.; Levi-Setti, R. *Int. J. Mass Spectrom. Ion Processes* **1995**, *143*, 191−212.
(28) Fragu, P.; Briançon, C.; Fourré, C.; Clerc, J.; Jeusset, J.; Halpern, S. *Microbeam Anal.* **1993**, *2*, 199−207.
(29) Burns, M. S. *J. Microsc.* **1982**, *127*, 237−258.
(30) Fragu, P.; Clerc, J.; Briançon, C.; Fourré, C.; Jeusset, J.; Halpern, S. *Micron* **1994**, *25*, 361−370.
(31) SIMS, A. e. i. i. d. t. b. *Biol. Cell* **1992**, *74*.
(32) Mathieu, H. J.; Léonard, D. *High Temp. Mater. Proc.* **1997**, *17*, 29−44.
(33) Wucher, A. *Fres. J. Anal. Chem.* **1993**, *346*, 3−10.
(34) Oechsner, H. *Int. J. Mass Spectrom. Ion Processes* **1995**, *143*, 271−282.
(35) Short, R. D.; Ameen, A. P.; Jackson, S. T.; Pawson, D. J.; O'Toole, L.; Ward, A. J. *Vacuum* **1993**, *44*, 1143−1160.
(36) Aller, A. J. *Appl. Spectros. Rev.* **1992**, *27*, 223−244.
(37) Migeon, H.-N.; Saldi, F.; Gao, Y.; Schuhmacher, M. *Int. J. Mass Spectrom. Ion Processes* **1995**, *143*, 51−63.
(38) Levi-Setti, R.; Fox, T. R. *Nucl. Inst. and Methods* **1980**, *168*, 139−149.
(39) Levi-Setti, R.; Hallégott, P.; Girod, C.; Chabala, J. M.; Li, J.; Sodonis, A.; Wolbach, W. *Surf. Sci.* **1991**, *246*, 94−106.
(40) Orloff, J.; Swanson, L. W.; Utlaut, M. *J. Vac. Sci. Technol. B* **1996**, *14*, 3759−3763.
(41) Sigmund, P. *Rev. Roum. Phys.* **1972**, *17*, 823−70, 969−1000, 1079−1106.
(42) Sigmund, P. *Sputtering by Particle Bombardment I*; Springer-Verlag: Berlin, 1981.
(43) Zandvliet, H. J. W.; Elswijk, H. B.; van Loenen, E. J.; Tsong, I. S. T. *Phys. Rev. B* **1992**, *46*, 7581−7587.
(44) Feil, H.; Zandvliet, H. J. W.; Tsai, M.-H.; Dow, J. D.; Tsong, I. S. T. *Phys. Rev. Lett.* **1992**, *69*, 3076−3079.
(45) Tsong, I. S. T.; Bedrossian, P. *Fundam. Processes Sputtering Atoms Mol.* **1992**, *Sput 92*, 209−222.
(46) Yu, M. L.; Reuter, W. *J. Vac. Sci. Technol.* **1980**, *17*, 36−39.
(47) Yu, M. L.; Reuter, W. *J. Appl. Phys.* **1981**, *52*, 1478−1498.
(48) Bryan, S. R.; Reich, F. *Poly Preprints* **1996**, *37*, 839−840.
(49) von Ardenne, M. In *Tabellen der Electronenphysik, Ionenphysik und Ubermikroskopie*; Deutscher Verlag der Wissenschaften: Berlin, 1956.
(50) Dookeran, N. N.; McMahon, J. M.; Short, R. T.; Todd, P. J. *Rapid Commun. Mass Spectrom.* **1995**, *9*, 1321−1324.
(51) Gillen, G.; Roberson, S. *Rapid Commun. Mass Spectrom.* **1998**, *12*, 1303−1312.
(52) Guilhaus, M. *J. Mass Spectrom.* **1995**, *30*, 1519−1532.
(53) Chabala, J. M.; Levi-Setti, R.; Wang, Y. L. *J. Vac. Sci. Technol. B* **1988**, *6*, 910−914.
(54) Benninghoven, A. *J. Vac. Sci. Technol. A* **1985**, *3*, 451−460.
(55) de Chambost, E.; Fercocq, P.; Fernandes, F.; Deloule, E.; Chaussidon, M. Secondary Ion Mass Spectrometry SIMS XI, 1997; pp 727−730.
(56) Williams, D. B.; Soni, K. K.; Tseng, M. W.; Chabala, J. M.; Levi-Setti, R. *J. Microsc.* **1993**, *169*, 163−172.
(57) Hurst, G. J.; Payne, M. G.; Kramer, S. D.; Young, J. P. *Rev. Mod. Phys.* **1983**, *51*, 767−819.
(58) Becker, C. H.; Gillen, K. T. *Appl. Phys. Lett.* **1984**, *45*, 1063−1065.
(59) Schühle, U.; Pallix, J. B.; Becker, C. H. *J. Am. Chem. Soc.* **1988**, *110*, 2323−2324.
(60) Terhorst, M.; Möllers, R.; Niehuis, E.; Benninghoven, A. *Surf. Int. Anal.* **1992**, *18*, 824−826.
(61) Brummel, C. L.; Willey, K. F.; Vickerman, J. C.; Winograd, N. *Int. J. Mass Spectrom. Ion Processes* **1995**, *143*, 257−270.
(62) Gersch, H.-U.; Wittmack, K. *J. Vac. Sci. Technol. A* **1993**, *11*, 125−135.
(63) Bieck, W.; Gnaser, H.; Oechsner, H. *Appl. Phys. Lett.* **1993**, *63*, 845−847.
(64) Kato, S.; Hamagaki, M.; Hara, T.; Aoyagi, K.; Namba, S.; Hayashi, S.; Yashior, H. *Nucl. Instrum. Methods Phys. Res.* **1988**, *B35*, 550−554.
(65) Freeman, S. P. H. T.; Ramsey, C. B.; Hedges, R. E. M. *Nucl. Instrum. Methods Phys. Res. B* **1994**, *92*, 231−236.
(66) Hedges, R. E. M.; Jiang, Z. X.; Ramsey, C. B.; Cowey, A.; Roberts, J. D. B.; Somogyi, P. *Nature* **1996**, *383*, 823−826.
(67) Valaskovic, G. A.; Morrison, G. H. *Scanning Microsc.* **1992**, *6*, 305−318.
(68) Jeusset, J.; Stelly, N.; Briançon, C.; Halpern, S.; Roshani, M.; Fragu, P. *J. Microsc.* **1995**, *179*, 314−320.
(69) Gillen, G.; Hues, S. M. *J. Am. Soc. Mass Spectrom.* **1993**, *3*, 419−423.
(70) Grasserbauer, M. *Pure Appl. Chem.* **1992**, *64*, 485−495.
(71) Wilhartitz, P.; Krismer, R.; Hutter, H.; Grasserbauer, M.; Weinbruch, S.; Ortner, H. M. *Fresenius J. Anal. Chem.* **1995**, *353*, 524−532.
(72) Brunner, C.; Hutter, H.; Piplits, K.; Gritsch, M.; Pöckl, G.; Grasserbauer, M. *Fresenius J. Anal. Chem.* **1998**, *361*, 667−671.
(73) Odom, R. W.; Grossbeck, M. L. *J. Mater. Res.* **1996**, *11*, 1923−1933.
(74) Scandurra, A.; Licciardello, A.; Torrisi, A.; La Mantia, A.; Puglishi, O. *J. Mater. Res.* **1992**, *7*, 2395−2402.
(75) Maternaghan, T. J.; Falder, C. J.; Levi-Setti, R.; Chabala, J. M. *J. Imaging Sci.* **1990**, *34*, 58−65.
(76) Chabala, J. M.; Levi-Setti, R.; Maternaghan, T. J. *J. Imaging Sci. Technol.* **1995**, *39*, 222−232.
(77) Verlinden, G.; Janssens, G.; Gijbels, R.; Van Espen, P.; Geuens, I. *Anal. Chem.* **1997**, *69*, 3772−3779.
(78) Prescott, R.; Mitchell, D. F.; Graham, M. J. *Corrosion Sci.* **1994**, *50*, 62−71.
(79) Prescott, R.; Mitchell, D. F.; Graham, M. J.; Doychak, J. *Corrosion Sci.* **1995**, *37*, 1341−1364.
(80) Clemens, D.; Bongartz, K.; Speier, W.; Hussey, R. J.; Quadakkers, W. J. *Fresenius J. Anal. Chem.* **1993**, *346*, 318−322.
(81) Brunner, C.; Hutter, H.; Wilhartitz, P.; Grasserbauer, M. *Microchim. Acta* **1997**, *126*, 69−72.
(82) Asuvathraman, R.; Rajagopalan, S.; Ananthasivan, K.; Mathews, C. K.; Mallya, R. M. *J. Nucl. Mater.* **1995**, *224*, 25−30.
(83) Lu, S. F.; Mount, G. R.; McIntyre, N. S.; Fenster, A. *Surf. Interface Anal.* **1994**, *21*, 177−183.
(84) Ramamurthy, S.; Walzak, T. L.; Lu, S. F.; Lipson, T. C.; McIntyre, N. S. *Surf. Interface Anal.* **1991**, *17*, 834−843.
(85) Takai, K.; Homma, Y. *Mater. Trans., JIM* **1995**, *36*, 1134−1139.
(86) Horita, T.; Yamaji, K.; Ishikawa, M.; Sakai, N.; Yokokawa, H. *J. Electrochem. Soc.* **1998**, *145*, 3196−3202.
(87) McIntyre, N. S.; Davidson, R. D.; Weisener, C. G.; Tayor, K. R.; Gonzalez, F. C.; Rasile, E. M.; Brennenstuhl, A. M. *Surf. Interface Anal.* **1992**, *18*, 601−603.
(88) Wang, Y. L.; Raval, A.; Levi-Setti, R. *Scanning Microsc.* **1989**, *3*, 731−737.
(89) Chabala, J. M. *Phys. Rev. B* **1992**, *46*, 11346−11357.
(90) Deimel, M.; Rulle, H.; Liebing, V.; Benninghoven, A. *Appl. Surf. Sci.* **1998**, *134*, 271−274.
(91) Soni, K. K.; Chabala, J. M.; Mogilevsky, R.; Levi-Setti, R.; Zhang, K.; Wolbach, W. S.; Bryan, S. R. *Surf. Interface Anal.* **1994**, *21*, 117−122.
(92) Wang, Y. L.; Levi-Setti, R.; Chabala, J. M.; Venkatesan, T.; Wu, X. D.; Inam, A.; Dutta, B. *J. Mater. Res.* **1989**, *4*, 1087−1092.
(93) Gillen, G.; Kaiser, D. L.; Wallace, J. S. *Surf. Interface Anal.* **1991**, *17*, 7−14.
(94) Thompson, A. M.; Soni, K. K.; Chan, H. M.; Harmer, M. P.; Williams, D. B.; Chabala, J. M.; Levi-Setti, R. *J. Am. Ceram. Soc.* **1997**, *80*, 373−376.
(95) Soni, K. K.; Thompson, A. M.; Harmer, M. P.; Williams, D. B.; Chabala, J. M.; Levi-Setti, R. *Appl. Phys. Lett.* **1995**, *66*, 2795−2797.
(96) Lampert, J. K.; Koermer, G. S.; Macaoay, J. M.; Chabala, J. M.; Levi-Setti, R. *Appl. Surf. Sci.* **1992**, *55*, 149−158.
(97) Chao, K.-J.; Lin, L.-H.; Ling, Y.-C.; Hwang, J.-F.; Hou, L.-Y. *Appl. Catal. A: Gen.* **1995**, *121*, 217−229.
(98) Ingo, G. M.; Padeletti, G. *Thin Solid Films* **1993**, *228*, 276−279.
(99) Ingo, G. M.; Padeletti, G. *Surf. Interface Anal.* **1994**, *21*, 450−454.
(100) Wolbach, W. S.; Bryan, S. R.; Shoemaker, G. L.; Krucek, T. W.; Maier, R. D.; Soni, K. K.; Chabala, J. M.; Mogilevsky, R.; Levi-Setti, R. *J. Mater. Sci.* **1997**, *32*, 1953−1961.
(101) Mogilevsky, R.; Bryan, S. R.; Wolbach, W. S.; Krucek, T. W.; Maier, R. D.; Shoemaker, G. L.; Chabala, J. M.; Soni, K. K.; Levi-Setti, R. *Mater. Sci., & Eng. A* **1995**, *191*, 209−222.
(102) Soni, K. K.; Chabala, J. M.; Mogilevsky, R.; Levi-Setti, R.; Tseng, M. W.; Williams, D. B. *JOM* **1993**, *45*, 29−33.

(103) Soni, K. K.; Tseng, M. W.; Williams, D. B.; Chabala, J. M.; Li, J.; Levi-Setti, R.; Bampton, C. C. *J. Microsc.* **1995**, *178*, 134−145.
(104) Diebold, A. C.; Lindley, P.; Viteralli, J.; Kingsley, J.; Liu, B. Y. H.; Woo, K.-S. *J. Vac. Sci. Technol. A* **1998**, *16*, 1825−1831.
(105) Childs, K. D.; Narum, D.; LaVanier, L. A.; Lindley, P. M.; Schueler, B. W.; Mulholland, G.; Diebold, A. C. *J. Vac. Sci. Technol. A* **1996**, *14*, 2392−2404.
(106) Gong, B.; Pigram, P. J.; Lamb, R. N. *Appl. Occup. Environ. Hyg.* **1996**, *11*, 782−789.
(107) Gong, B.; Pigram, P. J.; Lamb, R. N. *Int. J. Coal Geol*. **1997**, *34*, 53−68.
(108) Hou, X.; Ren, D.; Mao, H.; Lei, J.; Jin, K.; Chu, P. K.; Reich, F.; Wayne, D. H. *Int. J. Coal Geol*. **1995**, *27*, 23−32.
(109) Martin, R. R.; MacPhee, J. A.; Aye, K. T. *Energy Sources* **1989**, *11*, 105−112.
(110) Martin, R. R.; MacPhee, J. A.; Younger, C. *Energy Sources* **1989**, *11*, 1−8.
(111) Wang, Y. L.; Crow, G.; Levi-Setti, R.; Olsen, E. *Nucl. Instrum. Methods Phys. Res.* **1985**, *B10/11*, 716−718.
(112) Stephan, T.; Jessberger, E. K.; Klöck, W.; Rulle, H.; Zehnpfenning, J. *Earth Planet. Sci. Lett.* **1994**, *128*, 453−467.
(113) Mathez, E. A.; Mogk, D. M. *Am. Mineral.* **1998**, *83*, 918−24.
(114) Elphick, S. C.; Ngwenya, B. T.; Shimmield, G. B. *AAPG Bull. V* **1996**, *80*, 713−720.
(115) Guerquin-Kern, J.-L.; Coppey, M.; Carrez, D.; Brunet, A.-C.; Nguyen, C. H.; Rivalle, C.; Slodzian, G.; Croisy, A. *Microsc. Res. Technol.* **1997**, *36*, 287−295.
(116) Elphick, S. C.; Graham, C. M.; Walker, F. D. L.; Holness, M. B. *Mineral. Mag.* **1991**, *55*, 347−356.
(117) Brinen, J. S.; Greenhouse, S.; Nagaraj, D. R.; Lee, J. *Int. J. Miner. Processes* **1993**, *38*, 93−109.
(118) Brinen, J. S.; Reich, F. *Surf. Interface Anal.* **1992**, *18*, 448−452.
(119) Nagaraj, D. R.; Brinen, J. S. *Colloids Surf. A: Physicochem. Eng. Aspects* **1996**, *116*, 241−249.
(120) Hook, K. J.; Hook, T. J.; Wandass, J. H.; Gardella, J. A., Jr. *Appl. Surf. Sci.* **1990**, *44*, 29−41.
(121) Xu, K.; Proctor, A.; Hercules, D. M. *Int. J. Mass Spectrom. Ion Processes* **1995**, *143*, 113−129.
(122) Weng, L.-T.; Smith, T. L.; Feng, J.; Chan, C.-M. *Macromolecules* **1998**, *31*, 928−932.
(123) Dias, A. J.; Galuska, A. A. *Rubber Chem. Technol.* **1996**, *69*, 615−627.
(124) Briggs, D.; Fletcher, I. W.; Reichlmaier, S.; Agulo-Sanchez, J. L.; Short, R. D. *Surf. Interface Anal.* **1996**, *24*, 419−421.
(125) Marien, J.; Ghitti, G.; Jérôme, R.; Teyssié, P. *Polym. Bull.* **1993**, *30*, 435−440.
(126) Rouhi, A. M. *Chem. Eng. News* **1999**, *Jan. 18*, 51−59.
(127) Galuska, A. A. *Surf. Interface Anal.* **1997**, *25*, 790−798.
(128) Travaly, Y.; Bertrand, P. *Surf. Interface Anal.* **1995**, *23*, 328−334.
(129) Brummel, C. L.; Lee, I. N. W.; Zhou, Y.; Benkovic, S.; Winograd, N. *Science* **1994**, *264*, 399−402.
(130) Brummel, C. L.; Vickerman, J. C.; Carr, S. A.; Hemling, M. E.; Roberts, G. D.; Johnson, W.; Weinstock, J.; Gaitanopoulos, D.; Benkovic, S. J.; Winograd, N. *Anal. Chem.* **1996**, *68*, 237−242.
(131) Braun, R. M.; Blenkinsopp, P.; Mullock, S. J.; Corlett, C.; Willey, K. F.; Vickerman, J. C.; Winograd, N. *Rapid Commun. Mass Spectrom.* **1998**, *12*, 1246−1242.
(132) Hagenhoff, B.; Deimel, M.; Benninghoven, A.; Siegmund, H.-U.; Holtkamp, D. *J. Phys. D. Appl. Phys.* **1992**, *25*, 818−832.
(133) Leufgen, K. M.; Rulle, H.; Benninghoven, A.; Sieber, M.; Galla, H.-J. *Langmuir* **1996**, *12*, 1708−1711.
(134) Leufgen, K. M.; Rulle, H.; Galla, H.-J.; Sieber, M.; Benninghoven, A. Secondary Ion Mass Spectrometry (SIMS X), 1996; pp 797−800.
(135) Frisbie, C. D.; Martin, J. R.; Duff, R. R. J.; Wrighton, M. S. *J. Am. Chem. Soc.* **1992**, *114*, 7142−7145.
(136) Frisbie, C. D.; Wollman, E. W.; Martin, J. R.; Wrighton, M. S. *J. Vac. Sci. Technol. A* **1993**, *11*, 2368−2372.
(137) Frisbie, C. D.; Wollman, E. W.; Wrighton, M. S. *Langmuir* **1995**, *11*, 2563−2571.
(138) Tarlov, M. J.; Burgess, D. R. F., Jr.; Gillen, G. *J. Am. Chem. Soc.* **1993**, *115*, 5305−5306.
(139) Gillen, G.; Bennett, J.; Tarlov, M. J.; Burgess, D. R. F. J. *Anal. Chem.* **1994**, *66*, 2170−2174.
(140) Gillen, G.; Wight, S.; Bennett, J.; Tarlov, M. J. *Appl. Phys. Lett.* **1994**, *65*, 534−536.
(141) van der Wel, H.; van der Sluis-van der Voort, E.; Willard, N. P. *Surf. Interface Anal.* **1994**, *21*, 455−459.
(142) Gardner, T. J.; Frisbie, C. D.; Wrighton, M. S. *J. Am. Chem. Soc.* **1995**, *117*, 6927−6933.
(143) Gillen, G.; Wight, S.; Bright, D.; Herne, T. *Scanning* **1998**, *20*, 404−409.
(144) Wight, S.; Gillen, G.; Herne, T. *Scanning* **1997**, *19*, 71−74.
(145) Zimmerman, P. A.; Hercules, D. M.; Rulle, H.; Zehnpfenning, J.; Benninghoven, A. *Tappi J.* **1995**, *78*, 180−186.
(146) Brinen, J. S.; Kulick, R. J. *Int. J. Mass Spectrosc. Ion Processes* **1995**, *143*, 177−190.
(147) Ozaki, Y. *Nordic Pump Paper Res. J.* **1997**, *12*, 260−266.
(148) Patriot, C.; Jauneau, A.; Verdus, M. C.; Pobla, C.; Lefèbvre, F.; Demarty, M.; Thellier, M.; Ripoll, C. *J. Trace Microsc. Technol.* **1995**, *13*, 307−316.
(149) Grignon, N.; Halpern, S.; Jeusset, J.; Fragu, P. *JMSA* **1996**, *2*, 129−136.
(150) Lazof, D. B.; Goldsmith, J. K. G.; Rufty, T. W.; Suggs, C.; Linton, R. W. *J. Microsc.* **1994**, *176*, 99−109.
(151) Rihousey, C.; Jauneau, A.; Cabin-Flaman, A.; Demarty, M.; Lefèbvre, F.; Morvan, C. *Plant Physiol. Biochem.* **1995**, *33*, 497−508.
(152) Grignon, N.; Halpern, S.; Heusset, J.; Briancon, C.; Fragu, P. *J. Microsc.* **1997**, *186*, 51−66.
(153) Lhuissier, F.; Verdus, M. C.; Labulle, B.; Lefebvre, F.; Bocquel, C.; Ripoll, C. *Bot. Acta* **1997**, *110*, 378−387.
(154) Bailey, J. H. E.; Reeve, D. W. *J. Pulp Paper Sci.* **1996**, *22*, J274−J278.
(155) Bailey, J. H. E.; Reeve, D. W. *J. Pulp Paper Sci.* **1994**, *20*, J83−J86.
(156) Gea, L.; Jauneau, A.; Vian, B. *J. Trace Microsc. Technol.* **1994**, *12*, 323−329.
(157) Roy, S.; Gillen, G.; Conway, W. S.; Watada, A. E.; Wergin, W. P. *Protoplasma* **1995**, *189*, 163−172.
(158) Roy, S.; Jauneau, A.; Vian, B. *Plant. Physiol. Biochem.* **1994**, *32*, 633−640.
(159) Lazof, D. B.; Goldsmith, J. G.; Rufty, T. W.; Linton, R. W. *Plant Physiol.* **1996**, *112*, 1289−1300.
(160) Lazof, D. B.; Goldsmith, J. G.; Linton, R. W. *Progress in Botany*; Springer-Verlag: Berlin, 1997, Vol. 58, pp 112−149.
(161) Lazof, D. B.; Goldsmith, J. G.; Rufty, T. W.; Linton, R. W. *Plant. Physiol.* **1994**, *106*, 1107−1114.
(162) Chandra, S.; Morrison, G. H. *Biol. Cell* **1992**, *74*, 31−42.
(163) Ausserer, W. A.; Chandra, S.; Morrison, G. H. *J. Microsc.* **1989**, *154*, 39−57.
(164) Chandra, S.; Morrison, G. H.; Wolcott, C. C. *J. Microsc.* **1986**, *144*, 15−37.
(165) Stika, K. M.; Bielat, K. L.; Morrison, G. H. *J. Microsc.* **1980**, *118*, 409−420.
(166) Sod, E. W.; Crooker, A. R.; Morrison, G. H. *J. Microsc.* **1990**, *160*, 55−65.
(167) Mony, M. C.; Larras-Regard, E. *Biol. Cell* **1997**, *89*, 199−210.
(168) Chandra, S.; Morrison, G. H. *Int. J. Mass Spectrom. Ion Processes* **1995**, *143*, 161−176.
(169) Chandra, S.; Sod, E. W.; Ausserer, W. A.; Morrison, G. H. *Pure Appl. Chem.* **1992**, *64*, 245−252.
(170) Pacholski, M. L.; Cannon, D. M., Jr.; Ewing, A. G.; Winograd, N. *Rapid Commun. Mass Spectrom.* **1998**, *12*, 1232−1235.
(171) Colliver, T. L.; Brummel, C. L.; Pacholski, M. L.; Swanek, F. D.; Ewing, A. G.; Winograd, N. *Anal. Chem.* **1997**, *69*, 2225−2231.
(172) Cannon, D. M., Jr.; Pacholski, M. L.; Ewing, A. G.; Winograd, N. Secondary Ion Mass Spectrometry SIMS XI, 1997; pp 489−492.
(173) Cannon, D. M., Jr.; Pacholski, M. L.; Winograd, N.; Ewing, A. G. *Anal. Chem.*, submitted for publication.
(174) Smith, D. R.; Chandra, S.; Coderre, J. A.; Morrison, G. H. *Cancer Res.* **1996**, *56*, 4302−4306.
(175) Bennet, B. D.; Mumford-Zisk, J.; Coderre, J. A.; Morrison, G. H. *Radiat. Res.* **1994**, *140*, 72−78.
(176) Bennet, B. D.; Zha, X.; Gay, I.; Morrison, G. H. *Biol. Cell* **1992**, *74*, 105−108.
(177) Adovelande, J.; Boulard, Y.; Berry, J.-P.; Galle, P.; Slodzian, G.; Schrevel, J. *Biol. Cell* **1994**, *80*, 185−192.
(178) Clerc, J.; Halpern, S.; Fourre, C. l.; Omri, F.; Briancon, C.; Jeusset, J.; Fragu, P. *J. Nucl. Med.* **1993**, *34*, 1565−1570.
(179) Zhang, L. L.; Tardy, M.; Berry, J. P.; Escaig, F.; Galle, P. *Biol. Cell* **1992**, *74*, 99−104.
(180) Chandra, S.; Morrison, G. H. *J. Microsc.* **1997**, *188*, 182−190.
(181) Chandra, S.; Morrison, G. H.; Beyenbach, K. W. *Am. J. Physiol.* **1997**, *273*, F939−948.
(182) Chassard-Bouchaud, C.; Escaig, F.; Boumati, P.; Galle, P. *Biol. Cell* **1992**, *74*, 59−74.
(183) Lundgren, T.; Engström, E. U.; Levi-Setti, R.; Linde, A.; Norén, J. G. *J. Microsc.* **1994**, *173*, 149−154.
(184) Lundgren, T.; Chabala, J. M.; Levi-Setti, R.; Norén, J. G. *Histochem. J.* **1998**, *30*, 351−358.
(185) Bäckman, B.; Lundgren, T.; Engström, E. U.; Falk, L. K. L.; Chabala, J. M.; Levi-Setti, R.; Norén, J. G. *Acta Odontol. Scand.* **1993**, *51*, 79−89.
(186) Bushinsky, D. A.; Wolbach, W.; Sessler, N. E.; Mogilevsky, R.; Levi-Setti, R. *J. Bone Mineral Res.* **1993**, *8*, 93−102.
(187) Bushinsky, D. A.; Levi-Setti, R.; Coe, F. L. *J. Am. Physiol.* **1986**, F1090−F1097.
(188) Bushinsky, D. A.; Chabala, J. M.; Levi-Setti, R. *Am. J. Physiol.* **1990**, E586-E592.
(189) Bushinsky, D. A.; Sprague, S. M.; Hallegot, P.; Girod, C.; Chabala, J. M.; Levi-Setti, R. *J. Bone Mineral Res.* **1995**, *10*, 1988−1997.

(190) Bushinsky, D. A.; Gavrilov, K.; Stathopoulos, V. M.; Krieger, N. S.; Chabala, J. M.; Levi-Setti, R. *Am. J. Physiol.* **1996**, C1025−C1031.
(191) Chabala, J. M.; Levi-Setti, R.; Bushinsky, D. A. *Am. J. Physiol.* **1991**, F76−F84.
(192) Briançon, C.; Jeusset, J.; Halpern, S.; Fragu, P. *Microbeam Anal.* **1995**, *4*, 329−339.
(193) Fragu, P.; Francese, C.; Omri, F.; Jeusset, J. *Thyroid* **1994**, *4*, 203−208.
(194) Gerber, H.; Huber, G.; Peter, H. J.; Kämpf, J.; Lemarchand-Beraud, T.; Fragu, P.; Stocker, R. *Endocrinology* **1994**, *135*, 2688−2699.
(195) El May, M.; Jeusset, J.; El May, A.; Mtimet, S.; Fragu, P. *J. Clin. Endo. Metab.* **1996**, *81*, 2370−2375.
(196) Levi-Setti, R.; Chabala, J. M.; Smolik, S. *J. Microsc.* **1994**, *175*, 44−53.
(197) Levi-Setti, R.; Chabala, J. M.; Gavrilov, K.; Espinosa, R. I.; Le Beau, M. M. *Cell. Mol. Biol.* **1996**, *42*, 301−324.
(198) Levi-Setti, R.; Chabala, J. M.; Gavrilov, K.; Espinosa, R. I.; Le Beau, M. M. *Microsc. Res. Technol.* **1997**, *36*, 301−312.
(199) Levi-Setti, R.; Le Beau, M. *Biol. Cell* **1992**, *71*, 51−58.
(200) Bourgeois, C. A.; Dennebouy, R.; Gibaud, A.; Gerbault-Seureau, M.; Malfoy, B.; Slodzian, G.; Galle, P.; Dutrillaux, B. *Chromosome Res.* **1996**, *4*, 574−582.
(201) Todd, P. J.; McMahon, J. M.; Short, R. T.; McCandlish, C. A. *Anal. Chem.* **1997**, *69*, 529A-535A.
(202) McMahon, J. M.; Short, R. T.; McCandlish, C. A.; Brenna, J. T.; Todd, P. J. *Rap. Commun. Mass Spectrom.* **1996**, *10*, 335−340.
(203) Bayly, A. R.; Wolstenholme, J.; Petts, C. R. *Surf. Interface Anal.* **1994**, *21*, 414−417.
(204) Mouncey, S. P.; Moro, L.; Becker, C. H. *Appl. Surf. Sci.* **1991**, *52*, 39−44.
(205) Savina, M. R.; Lykke, K. R. *Anal. Chem.* **1997**, *69*, 3741−3746.
(206) Berthold, W.; Wucher, A. *Surf. Interface Anal.* **1995**, *23*, 393−398.
(207) Savina, M. R.; Lykke, K. R. *Trends Anal. Chem.* **1997**, *16*, 242−252.
(208) Willey, K. F.; Vorsa, V.; Braun, R. M.; Winograd, N. *Rapid Commun. Mass Spectrom.* **1998**, *12*, 1253−1260.
(209) Arlinghaus, H. F.; Spaar, M. T.; Switzer, R. C.; Kabalka, G. W. *Anal. Chem.* **1997**, *69*, 3169−3176.
(210) Gusev, A. I.; Vasseur, O. J.; Proctor, A.; Sharkey, A. G.; Hercules, D. M. *Anal. Chem.* **1995**, *67*, 4565−4570.
(211) Stoeckli, M.; Farmer, T. B.; Caprioli, R. M. *J. Am. Soc. Mass Spectrom.* **1999**, *10*, 67−71.
(212) Mehl, J. T.; Nicola, A. J.; Isbell, D. T.; Gusev, A. I.; Hercules, D. M. *Am. Lab.* **1998**, 30−38.
(213) van der Heide, P. A. W.; Karpuzov, D.; Khatamian, D. Secondary Ion Mass Spectrometry SIMS XI, 1997; pp 987−990.
(214) Lösing, R.; Reger, N.; Stadermann, F. J.; Ortner, H. M. Secondary Ion Mass Spectrometry SIMS XI, 1997; pp 1019−1022.
(215) Wu, K. J.; Odom, R. W. *Anal. Chem.* **1996**, *68*, 873−882.
(216) Liu, L. K.; Busch, K. L.; Cooks, R. G. *Anal. Chem.* **1981**, *53*, 109−113.
(217) Chatterjee, R.; Postawa, Z.; Winograd, N.; Garrison, B. J. *J. Phys. Chem.* **1999**, *103*, 151−163.

CR980137W